Comparison between Ultrasonic-Measurement-Integrated Simulation and Ordinary Simulation with Measured Upstream Velocity Condition

Shusaku SONE[1], Takaumi KATO[1], Kenichi FUNAMOTO[2], Toshiyuki HAYASE[2], Masafumi OGASAWARA[3],
Takao JIBIKI[3], Hiroshi HASHIMOTO[3], Kouji MIYAMA[3]

1 Graduate School of Biomedical Engineering, Tohoku University, 6-6-4 Aramaki Aza Aoba, Aoba-ku, Sendai 980-8579, JAPAN

2 Institute of Fluid Science, Tohoku University, 2-1-1 Katahira, Aoba-ku, Sendai 980-8577, JAPAN

3 GE Healthcare Japan, 4-7-127 Asahigaoka, Hino 191-8503, JAPAN

sone@reynolds.ifs.tohoku.ac.jp

ABSTRACT

In this study, UMI simulation and ordinary simulation with several upstream velocity boundary conditions were performed for blood flow in a carotid artery. The error of the UMI simulation was found to be almost half that of the ordinary simulation with measured upstream velocity condition, showing better accuracy in reproducing the blood flow.

1. Introduction

Development and progression of cardiovascular diseases is closely related to hemodynamics. As a novel technique to reproduce a blood flow field for advanced diagnosis, the authors have proposed and developed ultrasonic-measurement-integrated (UMI) simulation [1]. This method employs unsteady computation with feedback of errors in Doppler velocities, which are velocity components in the ultrasound beam direction of the blood flow, between ultrasonic measurement and computation to make the numerical result converge to the actual blood flow field, even if the accurate velocity profile at the upstream boundary is unknown. To date, we have constructed a two-dimensional UMI simulation system (Fig. 1) and shown the relationships between hemodynamic parameters based on the wall shear stress and pathology by investigating a number of clinical data of the carotid artery [2].

However, in the previous study, the accuracy between the UMI simulation and the ordinary simulation with a measured upstream velocity boundary condition was not compared. Thus, in the present study, we performed UMI simulation and ordinary simulation with several upstream velocity boundary conditions for a blood flow in a carotid artery to compare the accuracy of the results.

Fig. 1 Ultrasonic-Measurement-Integrated Simulation System

2. Method

The governing equations of UMI simulation are the Navier-Stokes equation (Eq. (1)) and the pressure equation (Eq. (2)) for incompressible and viscous fluid flow,

$$\rho\left(\frac{\partial \mathbf{u}}{\partial t} + (\mathbf{u} \cdot \nabla)\mathbf{u}\right) = \mu\Delta\mathbf{u} - \nabla p + \mathbf{f} \tag{1}$$

$$\Delta p = -\rho\nabla \cdot (\mathbf{u} \cdot \nabla)\mathbf{u} + \nabla \cdot \mathbf{f}, \tag{2}$$

where $\mathbf{u}$ is the velocity vector, p is the pressure, t is time, ρ is the density, μ is the dynamic viscosity, and $\mathbf{f}$ is the feedback signal. It is defined as an artificial body force proportional to the difference of Doppler velocities, V, between ultrasonic measurement and numerical simulation as follows:

$$\mathbf{f} = -K_v^* \frac{V_c - V_m}{U}\left(\frac{\rho U^2}{L}\right), \tag{3}$$

where K_v^* is the feedback gain (non-dimensional), U is the characteristic velocity, L is the characteristic length, and subscripts m and c represent the ultrasonic measurement and UMI simulation, respectively. The special case with $K_v^* = 0$ is the ordinary numerical simulation without feedback. The above governing equations were discretized by means of the finite volume method and were solved with the algorithm similar to the SIMPLER method.

The shape of the carotid artery was extracted by binarizing both time averaged color Doppler images and time averaged B mode images. The shape was then rotated so that the main direction of the blood flow would agree with the x-directional axis, and the computational grid was generated. The size of the computational grid is the same as the resolution of ultrasonic measurement, as Δx=280[μm] and Δy=170[μm], respectively. The objective was a blood flow in a carotid artery of an informed 76-years-old female patient. Ultrasound color Doppler images of 5 heart beats acquired with ultrasound diagnostic imaging equipment (LOGIQ7, GE Healthcare, JAPAN) with an
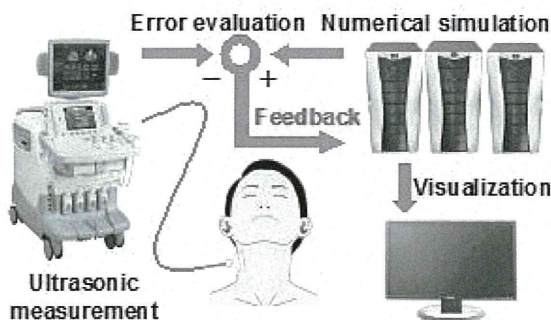
ultrasonic linear probe was used for analysis. The main frequency and repeated frequency were 5 MHz and 4.4 kHz, respectively. Feedback domain was set from 1/8 to 7/8 of the computational domain from the upstream. Feedback signals were added at each computational grid point in the feedback domain. The ordinary simulation was performed for the following upstream velocity boundary conditions:

(A) velocity profile with the measured Doppler velocity,

(B) velocity profile with the measured Doppler velocity scaled by flow rate estimation,

(C) parabolic velocity profile with flow rate estimation,

(D) uniform velocity profile with flow rate estimation.

UMI simulation was also performed with the same boundary conditions. The feedback gain was set to 100. The downstream boundary condition of all cases was free flow, and the no-slip condition was set on the wall. The blood flow rate was estimated to minimize the summation of the absolute value of the error between the measured and computed Doppler velocities in the feedback domain by means of the golden section method. The accuracy of the calculation was evaluated by the error norm defined as follows:

$$e = \frac{1}{N}\sum_n |V_c - V_m| / V_{\text{type}}, \qquad (4)$$

where V_{type} is typical Doppler velocity at the carotid artery.

3. Results and Discussion

Figure 2 shows a comparison between the ordinary simulation and the UMI simulation for Case (B). In the result for the ordinary simulation in Fig. 2(a), the velocity profile converges to a parabolic distribution in the downstream direction. On the other hand, the result of the UMI simulation in Fig. 2(b) shows downstream drift.

Next, the accuracy of the ordinary simulation and that of the UMI simulation were compared using the error norm of Eq. (4). In Fig. 3(a) for the ordinary simulation, the error norm of Case A was larger than those of the other cases. This implies that ultrasonic measurement in one cross section has some error in evaluating the flow rate. Comparing Cases B, C and D, the error norm of Case B is smallest. Also, for the UMI simulation in Fig. 3(b), the error norm in Case A was the largest, showing that applying the correct flow rate is important. The error norms for Cases B, C, and D are almost the same, implying that the UMI simulation is insensitive to the upstream boundary velocity profile. Comparison of Figs. 3 (a) and (b) shows that the error of the UMI simulation is almost half that of the ordinary simulation, revealing that the UMI simulation has a better accuracy than that of the ordinary simulation with measured upstream velocity condition.

4. Concluding remarks

In this study, UMI simulation and ordinary simulation with several upstream velocity boundary conditions were performed for a blood flow in a carotid artery. The error of the UMI simulation was found to be almost half that of the ordinary simulation with measured upstream

velocity condition, showing a better accuracy in reproducing the blood flow.
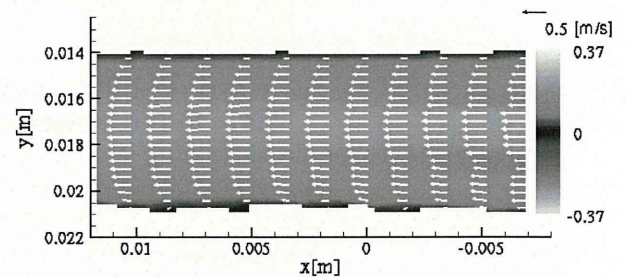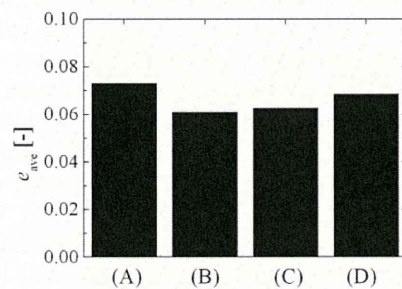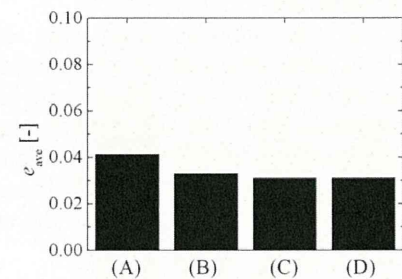

(a) Ordinary simulation.
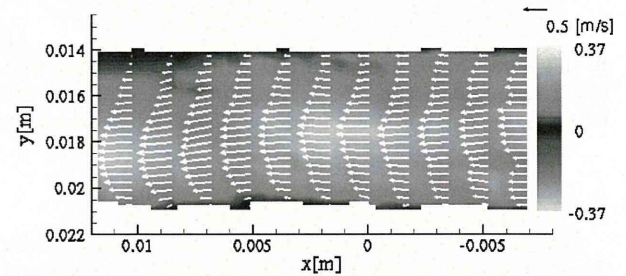
(b) UMI simulation

Fig. 2 Comparison of velocity fields for Case (B)

(a) Ordinary simulation.

(b) UMI simulation

Fig. 3 Comparison of error norm

References

[1] Funamoto K, et al. Fundamental Study of Ultrasonic -Measurement-Integrated Simulation of Real Blood Flow in the Aorta. *Ann Biomed Eng* **33**, 415-428, (2005).

[2] Kato T, et al. Evaluation of Wall Shear Stress on Carotid Artery with Ultrasonic-Measurement-Integrated Simulation. *Seventh International Conference on Flow Dynamics*, 542-543,(2010).

blood

In vivo imaging of the molecular distribution of the VEGF receptor during angiogenesis in a mouse model of ischemia

Yoh Hamada, Kohsuke Gonda, Motohiro Takeda, Akira Sato, Mika Watanabe, Tomoyuki Yambe, Susumu Satomi and Noriaki Ohuchi

Updated information and services can be found at:
http://bloodjournal.hematologylibrary.org/content/118/13/e93.full.html

Articles on similar topics can be found in the following Blood collections
    e-Blood (72 articles)
    Vascular Biology (335 articles)

Information about reproducing this article in parts or in its entirety may be found online at:
http://bloodjournal.hematologylibrary.org/site/misc/rights.xhtml#repub_requests

Information about ordering reprints may be found online at:
http://bloodjournal.hematologylibrary.org/site/misc/rights.xhtml#reprints

Information about subscriptions and ASH membership may be found online at:
http://bloodjournal.hematologylibrary.org/site/subscriptions/index.xhtml

e-Blood

In vivo imaging of the molecular distribution of the VEGF receptor during angiogenesis in a mouse model of ischemia

Yoh Hamada,[1,2] Kohsuke Gonda,[1] Motohiro Takeda,[1] Akira Sato,[2] Mika Watanabe,[3] Tomoyuki Yambe,[4] Susumu Satomi,[2] and Noriaki Ohuchi[1,5]

[1]Department of Nano-Medical Science, Graduate School of Medicine, Tohoku University, Sendai, Japan; [2]Department of Advanced Surgical Science and Technology, Graduate School of Medicine, Tohoku University, Sendai, Japan; [3]Department of Pathology, Tohoku University Hospital, Sendai, Japan; [4]Department of Medical Engineering and Cardiology, Institute of Development, Aging and Cancer, Tohoku University, Sendai, Japan; and [5]Department of Surgical Oncology, Graduate School of Medicine, Tohoku University, Sendai, Japan

Vascular endothelial growth factor (VEGF) plays a critical role in angiogenesis and has been applied to medical therapy. However, because vascular imaging at the molecular level is impossible, the detailed in vivo dynamics of VEGF and its receptor (VEGFR) remain unknown. In this study, to understand the molecular distribution of VEGF and the VEGFR, we prepared ischemic mice with a new surgical method and induced angiogenesis in the gastrocnemius muscle. Then, we made a VEGF-conjugated fluorescence nanoparticle and performed staining of VEGFR-expressing cells with the fluorescent probe, demonstrating the high affinity of the probe for VEGFR. To observe the physiologic molecular distribution of VEGFR, we performed in vivo single-particle imaging of gastrocnemius in the ischemic leg with the fluorescent probe. The results suggested that only a 3-fold difference of VEGFR distribution is involved in the formation of branched vasculature in angiogenesis, although previous ex vivo data showed a 13-fold difference in its distribution, indicating that a method inducing a several-fold local increase of VEGFR concentration may be effective in generating site-specific angiogenesis in ischemic disease. This new in vivo imaging of ischemic mice could make useful contributions to understanding the mechanisms of angiogenesis and to developing a VEGFR-related drug. (*Blood*. 2011;118(13): e93-e100)

Introduction

Angiogenesis and arteriogenesis play a critical role in neovascularization in adults.[1] Angiogenesis is defined as the sprouting of new capillaries from postcapillary venules,[2] whereas arteriogenesis is defined as the process of artery maturation or the de novo growth of collateral conduits.[3] Our laboratory studies the mechanisms of angiogenesis, and clarification of these mechanisms is crucial for the development of new treatments for arteriosclerotic disorders. Recently, medical applications for recombinant vascular endothelial growth factor (VEGF) proteins or genes have been developed.[4] However, no placebo-controlled trial has yielded overwhelmingly positive results.[1] An understanding of the detailed molecular mechanisms of this angiogenesis factor in vivo is thought to be very important for the effective design of a VEGF-related drug delivery system. However, neither VEGF activity nor VEGFR distribution has been quantitatively analyzed in vivo at a molecular level with respect to therapeutic angiogenesis. In previous animal studies, the efficacy of treatment for atherosclerotic disease was primarily evaluated using angiography, laser Doppler imaging, and the determination of histologic capillary density.[5,6] Angiography can be used to noninvasively visualize vessel size, vessel branching, and the vascular network throughout the body. However, because it is difficult to visualize vascular structures several hundred micrometers beneath the imaging surface, this method is not adequate for the observation of early-stage angiogenesis at a

molecular level. Laser Doppler imaging provides a noninvasive measurement of blood flow by determining the Doppler frequency shift of reflected light because of the motion of red blood cells. This technique enables quantitative analysis of improvements in blood flow after injury to the vasculature. However, the Doppler shift measurement is easily influenced by movement artifacts, room temperature, and blood pressure.[7] In addition, it is difficult to analyze microvascular structures using laser Doppler imaging because the resolution of the obtained image is limited by diffusion of the reflected light because of distance between the red blood cells and the detector. Histologic measurements of capillary density can reveal quantitative increases in blood vessel density, and many previous studies have used this metric as a standard evaluation of angiogenesis. However, continuous observation of the same tissue is impossible with this measurement technique as protein structure is influenced by fixation of the tissues. For this reason, histologic techniques are not recommended for physiologic observations of the angiogenesis process. In the aforementioned methods, as resolution is limited to the micrometer level and imaging at the molecular level is currently impossible, the detailed in vivo dynamics of individual VEGF and VEGF receptor (VEGFR) molecules remain unknown. We have developed an in vivo single-particle imaging system using bright and photo-stable fluorescent nanoparticles, or quantum dots (QDs), with a spatial
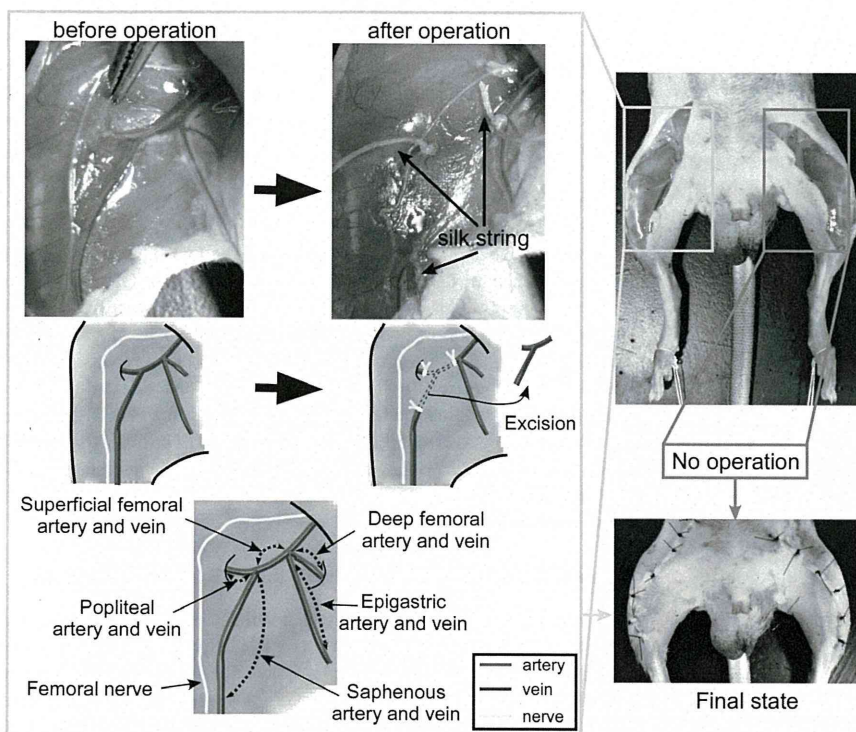
Figure 1. Procedure for preparing the hemi-hind limb ischemic mouse model. On the right leg, we ligated the proximal end of the superficial femoral artery and vein, the origins of the popliteal artery and vein, and the distal portions of the saphenous artery and vein with surgical silk. All vessels surrounding the 3 ligated points were excised. The left leg was not treated, except for an incision in the skin of the thigh.

precision of 7-9 nm. This was performed to clarify the molecular mechanisms of an anti-HER2 antibody-based drug delivery system and of cancer metastasis in tumor-bearing mice.[8,9]

The use of an ischemic mouse model is highly effective for understanding the in vivo molecular dynamics of angiogenic factors and their effects on vascular remodeling. However, 2 surgical concerns impose limitations on previous mouse models.[10] First, angiogenesis and arteriogenesis were not separately evaluated in previous models. As both processes contribute to an increase in the rate of blood flow,[1] it is necessary that the effects of arteriogenesis be eliminated if angiogenesis is to be analyzed. Second, inflammation and edema at the surgical site are known to affect angiogenesis.[11] To overcome these problems, it is critical to establish an improved ischemic mouse model that selectively induces angiogenesis at a specific muscle. Here, we demonstrate the development of an imaging method for determining the molecular distribution of VEGFR labeled with QD-conjugated VEGF. This technique was designed to observe angiogenesis in a novel ischemic mouse model that induces angiogenesis in the gastrocnemius. Our results suggest that only a several-fold difference in VEGFR distribution is required for the promotion of angiogenesis. This novel imaging method may aid in the development of drugs and treatments for atherosclerotic diseases.

Methods

Animals

C57BL/6J male mice (Charles River Laboratories) weighing 20-27 g and 8-9 weeks of age were used for all experiments. All surgical processes were performed under anesthesia with ketamine (100-120 mg/kg) and xylazine (8-10 mg/kg). Anesthesia was maintained for the course of the imaging session. Animals were used in accordance with guidelines approved by the committee on animal experiments of Tohoku University.

Hemi-hind limb ischemic mouse model

The hair of each mouse was removed from the abdomen and both hind limbs with an electric shaver and depilatory cream. The skin from both thighs was then incised to expose the arteries, veins, and nerves. To induce selective ischemia in the gastrocnemius, which is located in the deep layer of the thigh muscles, 3 vessels of the femoral area were ligated in the right hind limb. First, the proximal end of the superficial femoral artery and vein were ligated with surgical silk, size 6-0. Second, the origins of the popliteal artery and vein were ligated. Third, the distal portions of the saphenous artery and vein were ligated to avoid the backflow of blood. Femoral nerves were carefully preserved. Each of the vessels that were surrounded by the 3 ligated points was excised. The left leg was not treated, except for an incision in the skin of the thigh. Finally, the overlying skin was closed (Figure 1).

Histologic capillary density

To confirm that the surgical operation-induced angiogenesis in the gastrocnemius, we performed immunohistologic staining of the muscle with anti-CD31 antibody, a marker for vascular endothelial cells. Mice were killed at predetermined times (7, 14, 21, and 28 days after operation). The gastrocnemius was removed and fixed overnight in 10% formalin in PBS. After fixation, the tissue was embedded in paraffin, and the tissue sections were prepared and mounted on slides. The tissue samples were deparaffinized, and antigen retrieval was performed with proteinase K treatment. After this treatment, the tissue samples were incubated with a rat anti-CD31 monoclonal primary antibody (Angio-Proteomie) at 5 μg/mL for 12 hours at 4°C. After being washed with PBS, the samples were incubated with a biotinylated antirat IgG secondary antibody (Vector Laboratories; 100-fold dilution) for 30 minutes at 25°C. After incubation, the samples were incubated with HRP-conjugated streptavidin (Nidchirei) for 30 minutes at 25°C. Samples were then treated with diaminobenzidine chromogen reagent (Dojindo) and counterstained with hematoxylin. The samples were observed using light microscopy (BX51; Olympus) with an objective lens (×40, 0.75 NA; Olympus) and a camera (DP-25B; Olympus). The images were acquired with image processing software (DP2-BSW Version 1.2).

Laser Doppler perfusion imaging

Blood perfusion of the hind limb was measured using a Laser Doppler Perfusion Imaging system (MoorLDI2-IR; Moor Instruments). This imaging technique provides a noninvasive measurement of blood flow by determining the Doppler frequency shift of light reflected off of moving red blood cells. Mice under the same anesthetic dose described in "Animals" were scanned from the lower abdomen to the end of the toes. After scanning, colored images were obtained with original software (RE-SEARCH Version 3.09; Moor Instruments). Each pixel in the acquired images reflected an original blood flow value, referred to as a perfusion unit (PU). The mean of the PUs of the lower thighs in a control limb and a treated hind limb was determined. The PUs of ischemic legs were obtained at different time points (before operation, soon after operation, and 7, 14, 21, and 28 days after operation). The relative ratios of the mean PUs between the ischemic and control legs in the same mouse were calculated.

Cell lines

A pancreatic islet endothelial mouse cell line, MS1, was obtained from ATCC. MS1-VEGF cells, which express VEGFR on the cell membrane via the transfection of the VEGF gene, were also acquired from ATCC. These cells were cultured in DMEM (Invitrogen) supplemented with 5% FBS.

Immunostaining of cultured cells with an anti-VEGFR antibody

MS1 and MS1-VEGF cells were cultured on slide glass chambers. After 3 days, the slides were placed in 2.5% formalin in DMEM for 10 minutes. After fixation, the cells were incubated with an anti–mouse VEGFR monoclonal antibody (Pierce Chemical) or a whole mouse IgG (Rockland) primary antibody at 10 µg/mL for 12 hours at 25°C. After the samples were washed with PBS, the cells were incubated with a HRP-conjugated anti–mouse IgG secondary antibody (KPL Europe; 100-fold dilution) for 1 hour at 25°C. After incubation, the samples were treated with diaminobenzidine chromogen reagent and counterstained with hematoxylin. We observed the samples with the same optical system in "Histologic capillary density."

Preparation of angiogenesis factor-conjugated QDs

Mouse VEGF 164 (R&D Systems) and platelet-derived growth factor BB (PDGF; Biovision) were biotinylated using the EZ-Link Micro Sulfo-NHS-LC-Biotinylation Kit (Pierce Chemical). In this reaction, a 1:50 molar ratio of angiogenesis factors and Sulfo-NHS-LC-Biotin was used according to the manufacturer's instructions. The biotinylated VEGF and PDGF were then mixed with avidin-conjugated Qdot705 nanoparticles (QD705; Invitrogen) at a molar ratio of 8:1 or 16:1 and incubated for 1 hour at 25°C. The number of QD705 nanoparticles determined the emission wavelength. QD705-conjugated VEGF and PDGF were termed VEGF-QD and PDGF-QD, respectively.

Single-particle imaging system

The optical system used to observe the fluorescence of the angiogenesis factor-conjugated QDs consisted primarily of an epifluorescent microscope (IX-71; Olympus), a Nipkow disk-type confocal unit (CSU10; Yokogawa), and an EMCCD camera (Ixon DV887; Andor). An objective lens (60×, PlanApo, 1.40 NA; Olympus) was used for imaging. VEGF-QDs were illuminated using a green laser (532 nm; Spectra-Physics). The laser-excited fluorescence of the QDs was filtered with a 695- to 740-nm band-pass filter. Images were obtained at a rate of 5 frames/second. For in vivo imaging, to remove the oscillation because of heartbeats and respiration, a gastrocnemius window was developed and attached to the aforementioned microscopy system.

Single-particle imaging of VEGF-QDs in cultured cells

To investigate the affinity of VEGF-QDs for VEGFR, MS1, and MS1-VEGF, cells were incubated with 1, 10, or 50nM VEGF-QDs for 1 hour at 25°C. After 3 washes with DMEM, these cells were observed in a glass-bottom dish using the single-particle imaging system. The fluores-

cence intensities of QD signals from the cells were analyzed as gray values using ImageJ 1.38 software (www.rsb.info.nih.gov/ij). The gray values of 100 frames (200 milliseconds/frame) from a single cell were averaged, and the gray value of the background was subtracted from that of the cell. The mean gray value per pixel in the background-subtracted image of the cell was multiplied by the total number of pixels making up the image of the cell. The total fluorescence intensity of the QDs per cell was thus determined. In the 10nM VEGF-QD treatment, QD fluorescence signals were clearly observed on MS1-VEGF cells. In contrast, when MS1-VEGF cells were incubated with 1nM VEGF-QDs, the QD fluorescence signals were low. When the cells were treated with 50nM VEGF-QDs, QD signals were exceedingly high or even saturated (data not shown). In MS1 cells incubated with various concentrations of VEGF-QDs, the VEGF-QD fluorescence signals were very low. These results indicate that VEGF-QDs specifically recognize VEGFR and that the 10nM concentration was appropriate for imaging the binding of VEGF-QDs to VEGFR. Moreover, to provide stronger evidence of the affinity of VEGF-QDs for VEGFR, MS1, and MS1-VEGF, cells were incubated with 10nM unconjugated QDs, PDGF-QDs, or VEGF-QDs for 1 hour at 25°C, and the resulting fluorescence intensities were examined.

In vivo fluorescence imaging with the IVIS Spectrum system

To confirm that VEGF-QDs accumulated in the ischemic leg, we performed in vivo fluorescence imaging using the IVIS Spectrum imaging system (Caliper Life Sciences) at 4, 9, and 14 days after preparation of ischemic model mice. Unconjugated QDs or VEGF-QDs were injected intracardially into the mice. The final concentration of the QD probes in the blood was 10nM, as determined by the single-particle imaging data from cultured cells. The detection sensitivity of the fluorescent signal using the IVIS Spectrum is poorer than the single-particle imaging system but allows for noninvasive visualization of the whole body of the mouse. Therefore, fluorescence images were taken 10 minutes after injection of fluorescent probes, before the fluorescence signals decreased, because of their washing out with the blood. Fluorescence intensities of the QDs were analyzed using accessory software (Living Image Version 4.0; Caliper Life Sciences). For data analyses, the relative ratio of fluorescence between the ischemic and control leg of the same mouse was calculated.

Single-particle imaging of VEGF-QDs in the gastrocnemius of ischemic model mice

To examine the distribution of VEGF-QDs in the gastrocnemius of the ischemic leg, we performed in vivo single-particle imaging of the vasculature 4, 9, and 14 days after operation. The skin of the ischemic leg was opened to expose the thigh muscles. The skin of the hind limbs was then fixed to a plastic plate using suture thread and Superglue. Use of Superglue made both connections of the skin to the plate more stable without damaging the vasculature, eliminating the background oscillations from the heartbeat and respiration during observation. To expose the gastrocnemius, the skin and hemimembranous muscle, which is located on the superficial layer of the gastrocnemius, were then removed. The mouse, which was mounted as described on the plastic plate, was then fixed to a hand-made aluminum stage designed to stabilize the plate with screws. Unconjugated QDs or VEGF-QDs were injected intracardially into the mice. The sensitivity of the single-particle imaging system to the fluorescence signal is extremely high; and immediately after injection, a part of probes are free in the blood and have not bound to VEGFR. This initially prevents observation of the interaction between the VEGF-QDs and VEGFR on the vascular wall. Therefore, in vivo single-particle imaging of the fluorescent probes was carried out 1 hour after injection. By this time, the concentration of the free probe in the blood was decreased. To quantitatively measure the affinity of the VEGF-QDs for the vasculature, an analysis was performed as follows. A total of 100 frames, each 512 pixels square and representing an exposure of 200 milliseconds, were overlaid using image processing software (G-count 1.01; G-angstrom). A portion of the overlaid (192 pixels square) image was examined to determine the number of QD particles in proper-sized vasculature. For each image analyzed, the fluorescence intensity (as gray values) of QD signals from the tissues was determined using ImageJ software. The mean gray value, derived from the tissues'
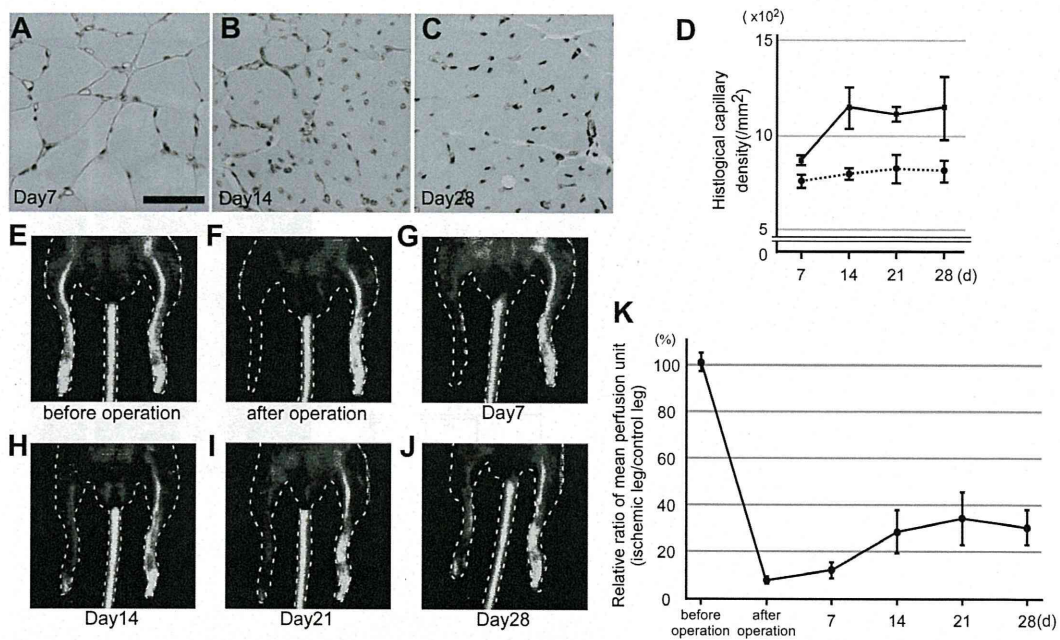
Figure 2. Evaluation of angiogenesis of the ischemic model mice. (A-C) Typical images of the gastrocnemius immunostained with an anti-CD31 antibody. The muscles from ischemic legs were isolated at 7, 14, and 28 days after the induction of ischemia and immunostained. Brown circles and dots represent CD31$^+$ capillaries. Scale bar represents 50 μm. (D) Measurement of CD31$^+$ capillary density. In the gastrocnemius of the ischemic or control leg, capillaries stained with the anti-CD31 antibody were counted. Solid and dotted lines represent the sample derived from ischemic and control legs, respectively. n = 4. Error bars represent SEM. (E-J) Changes in blood perfusion were assessed using laser Doppler perfusion imaging in ischemic legs of model mice. (E-F) Images before and soon after operation. After operation, the perfusion signal in the ischemic leg is significantly decreased. (G-J) Images from 7, 14, 21, and 28 days after operation. Blood perfusion in an ischemic leg gradually increases. (K) Change in perfusion units as determined by this imaging technique. Relative ratios of mean perfusion units between ischemic and control legs in the same mouse are shown (ischemic leg value/control leg value). n = 6. Error bars represent SEM.

autofluorescence per pixel, was subtracted from the fluorescence value of the vascular wall area. The resulting gray value was then multiplied by the total number of pixels of the vascular wall. This value reflected the total fluorescence intensity of all QDs bound to the vascular wall (total QD value).

To precisely determine the number of QD particles on the vascular wall, it was necessary to define the fluorescence intensity of a single QD. Because QDs that fluoresce at the same wavelength are uniform in size, QD705 fluorescence intensity is proportional to the particle number. Moreover, the QD fluorescence is composed of fluorescent and nonfluorescent states referred to as on- and off-states. This property results in blinking of a QD. When the fluorescence and other properties of QD particles were analyzed immediately after their purchase, we determined that the mean duration of the off-state over 20 seconds was approximately 4 seconds and that the calculated SEM was very low.[12] In cases where QDs aggregate, the mean duration of the off-state per unit time is shortened because the on- and off-states of each particle in the aggregate occur randomly. Therefore, based on an off-state duration of 4 seconds, we selected a single particle QD from each image and measured the fluorescence intensity of the single QD particle (single QD value) in the same manner as the total QD value. The total QD value was divided by a single QD value, and the number of QD particles per 10 μm of vascular wall was calculated.

Statistical analysis

Data are mean $\pm$ SEM. An F test was performed and equal variance was defined as P values $\geq$ .05. Comparisons between groups were performed using the parametric Student t test ($\geq$ .05 at F test) or Welch t test ($P <$ .05 at F test). $P <$ .05 was considered significant for both t tests.

Results

Induction of angiogenesis in ischemic model mice

To induce angiogenesis at a selected site and to eliminate the effects of inflammation and edema,[11] we targeted the gastrocnemius. This

muscle is primarily supplied by the popliteal and saphenous arteries, and no remarkable collateral arteries exist near the muscle. We therefore ligated the popliteal and saphenous arteries to induce angiogenesis in the gastrocnemius (Figure 1). Other muscles in the thigh are primarily supplied by the deep femoral artery, which was maintained as a collateral artery after the surgery. Therefore, we think that our surgery is appropriate for analyses of angiogenesis mechanisms. The gastrocnemius is located deep among the thigh muscles, and the skin and semimembranosus muscle located on the upper layer of the gastrocnemius were removed just before in vivo imaging. Therefore, we avoided the effects of inflammation and edema-induced factors on normal angiogenesis. To determine whether the number of capillaries in the gastrocnemius of ischemic legs increased, we histologically determined the capillary densities over time (Figure 2A-C). Capillary densities in the control legs did not significantly change during observation (Figure 2D). In contrast, the capillary densities in ischemic legs increased gradually over 14 days, peaked at day 14, and were steady between day 14 and day 28. This finding demonstrates that angiogenesis was induced in the ischemic leg (Figure 2D). To investigate improvement of blood flow in the model mice using another method, we evaluated the change in blood flow using laser Doppler perfusion imaging (Figure 2E-J). The relative ratio of the mean PU between ischemic and control legs in the same mouse (ischemic leg value/control leg value) decreased to $\sim$ 8% soon after operation (Figure 2E-F,K). This ratio then increased to $\sim$ 34% 21 days after the surgery (Figure 2I,K). Both observations indicate that angiogenesis was effectively induced in the gastrocnemius between 7 days and 14 days after the procedure. The slight difference in the rate of increase of perfusion between the 2 imaging methods may be because the laser Doppler perfusion imaging analyzed the thigh as a whole, and arteriogenesis induced by inflammation and

Figure 3. VEGFR distribution in MS1 and MS1-VEGF cells and the affinity of angiogenesis factor-conjugated QDs to these cell lines. (A-D) Immunostaining of MS1 and MS1-VEGF cells with an anti-VEGFR antibody. Scale bar represents 50 μm. (E-H) Typical images of cells treated with fluorescent particles. MS1 and MS1-VEGF cells were treated with unconjugated QDs, PDGF-QDs, or VEGF-QDs. Representative images are shown of cells treated with PDGF-QDs and VEGF-QDs. Data from cells treated with unconjugated QDs are not shown. White dots represent fluorescent QDs; and white dotted lines, the outline of the cell. Scale bar represents 10 μm. (I) QD fluorescence intensity per cell. The fluorescence intensity of QD signals from the cells was analyzed as gray values. In each condition, n = 30. **$P < .01$. Error bars represent SEM.
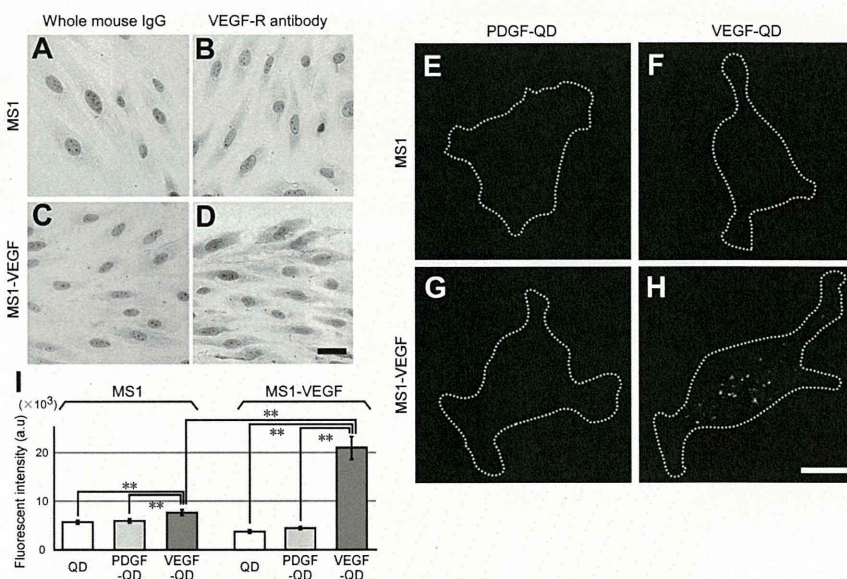
edema of the semimembranous muscle may have occurred in this larger volume.

Preparation and characterization of VEGF-QDs

To visualize the molecular distribution of VEGF using single-particle imaging, VEGF was conjugated with QDs (VEGF-QD). PDGF-conjugated QDs (PDGF-QD) were also prepared as control probes (supplemental Figure 1, available on the *Blood* Web site; see the Supplemental Materials link at the top of the online article). To examine the binding of VEGF-QD and VEGFR, staining was performed on MS1 and MS1-VEGF cells treated with unconjugated QDs, PDGF-QDs, and VEGF-QDs. High levels of VEGFR expression in MS1-VEGF cells were confirmed by immunostaining with an anti-VEGFR antibody (Figure 3C-D), whereas low-level expression was observed in MS1 cells (Figure 3A-B). The analyses of QD-probe fluorescence indicated that the total fluorescence intensity of VEGF-QDs in MS1-VEGF cells was $21.0 \pm 2.4 \times 10^4$ (Figure 3H-I). This value was remarkably higher than the observed fluorescence values of stained MS1-VEGF cells treated with unconjugated QDs or PDGF-QDs (unconjugated QDs, $3.8 \pm 0.3 \times 10^4$; PDGF-QDs, $4.4 \pm 0.3 \times 10^4$; Figure 3G,I) and those of MS1 cells treated with unconjugated QDs, PDGF-QDs, or VEGF-QDs (unconjugated QDs, $5.7 \pm 0.4 \times 10^4$; PDGF-QDs, $6.0 \pm 0.4 \times 10^4$; VEGF-QDs, $7.7 \pm 0.6 \times 10^4$; Figure 3E-F,I). These results demonstrate that VEGF-QDs bind specifically to VEGFR.

In vivo distribution of VEGFR labeled with VEGF-QDs

To determine the distribution of VEGFR labeled with VEGF-QDs during angiogenesis, we performed 2 in vivo fluorescence imaging techniques. In these imaging protocols, we examined ischemic model mice at 4, 9, and 14 days after operation to analyze in detail the changes in VEGFR distribution over time. Imaging performed with the IVIS Spectrum system has the advantage of imaging the fluorescence of the entire body of the mouse, although the spatial precision of this technique is low. To simultaneously observe the fluorescence of both ischemic and control legs after injection of unconjugated QDs or VEGF-QDs into the model mice, the IVIS Spectrum system was used (Figure 4A-D). Individual mice exhibit different degrees of autofluorescence. The relative ratio of fluores-

cence between the ischemic and control leg in each mouse was therefore calculated (ischemic leg fluorescence/control leg fluorescence). In model mice at 4 days after operation, the relative fluorescence ratio resulting from injection of unconjugated QDs was 0.71 ± 0.01, and the ratio after injection of VEGF-QDs was 0.72 ± 0.03 (Figure 4E). These results indicate that VEGF-QDs did not selectively accumulate in the ischemic legs at the time of
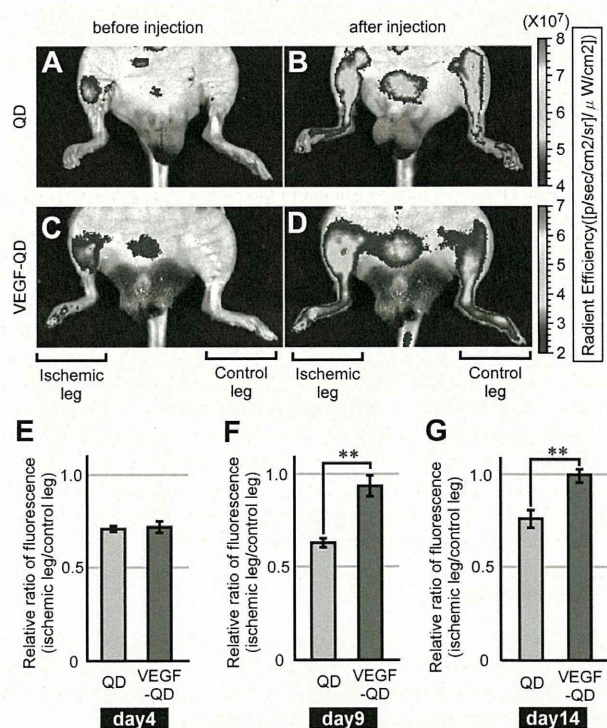

Figure 4. In vivo fluorescence imaging of the ischemic model mice using the IVIS Spectrum system. (A-D) Images using IVIS Spectrum. Unconjugated QDs and VEGF-QDs were injected intracardially into the model mice. Mice were illuminated with light with a wavelength of 625-655 nm. Excited fluorescence was filtered with a 690- to 710-nm wavelength band-pass filter. (E-G) The relative ratios of fluorescence between ischemic and control legs in mice at 4 days (E), 9 days (F), and 14 days (G) after operation. The fluorescence intensity of the ischemic leg divided by that of the control leg was calculated (ischemic leg fluorescence/control leg fluorescence). n = 5. Error bars represent SEM. **$P < .05$.
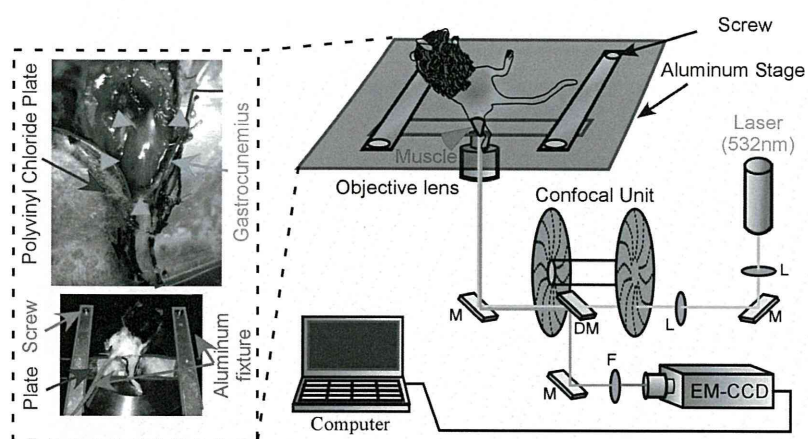
Figure 5. Schematic of the in vivo single-particle imaging system. An ischemic leg of a model mouse was stabilized on a polyvinyl plate using suture thread and instant Superglue. The skin and hemimembranous muscle were then removed. The gastrocnemius was selectively imaged using a single-particle imaging system.

measurement. In contrast, at 9 and 14 days after operation, the relative ratios resulting from injection of unconjugated QDs were 0.65 ± 0.02 and 0.76 ± 0.05, respectively, whereas the observed ratios after injection of VEGF-QDs were 0.94 ± 0.06 and 1.00 ± 0.04, respectively (Figure 4F-G), suggesting that VEGF-QDs accumulated in the ischemic leg to a greater degree than in the control leg at the time of measurement.

In addition to using the IVIS system, we also conducted in vivo single-particle imaging. For this protocol, we developed surgical fixation methods of mice beyond that in our previous imaging method. In particular, we designed a polyvinyl chloride plate with a window fit to the shape of the gastrocnemius. The skin around the gastrocnemius was bound to the plate with suture thread and Superglue (Figure 5). These improvements eliminated background oscillations because of the heartbeat and respiration, enabling us to observe the physiologic angiogenesis that sustains blood flow after ischemia (supplemental Movies 1, 2). We observed the distribution of unconjugated QDs or VEGF-QDs after injection of the respective probe. The results indicate that a large number of VEGF-QDs were specifically localized on the vessel walls in ischemic legs (Figure 6A-H), whereas fluorescence after injection of unconjugated QDs was very weak (supplemental Figure 2A-D). We measured the total fluorescence intensity resulting from all QDs on the vascular wall (total QD value) and the fluorescence intensity of single QD (single QD value) as gray values. The total QD value was then divided by the single QD value, and the number of QD particles per 10 μm of the vascular wall was calculated (Figure 6I; supplemental Figure 2E). These analyses revealed that QD fluorescence on the vascular wall was weak in both ischemic and control legs in mice injected with unconjugated QDs (supplemental Figure 2E). When VEGF-QDs probe were injected at 4 days after operation, the number of VEGF-QDs on the vascular walls of ischemic legs was similar to the number observed in control legs. Moreover, there was no difference in number of particles on the walls of branched or linear vasculature in ischemic legs (Figure 6C-D,I). In contrast, the number of VEGF-QDs in the branched vasculature in ischemic legs was 3.4-fold greater than the number of VEGF-QDs in the linear vasculature 9 days after operation (Figure 6E-F,I) and 4.5-fold greater than the number of VEGF-QDs in the branched vasculature in control legs (Figure 6B,F,I). Fourteen days after operation, the number of VEGF-QDs on the walls of the branched vasculature in ischemic legs was 3.3-fold greater than the number of particles on the walls of the linear vasculature (Figure 6G-I) and 4.3-fold greater than the number of

VEGF-QDs in the branched vasculature in control legs (Figure 6I). These results demonstrate that our single-particle imaging method is able to quantitatively describe the in vivo distribution of VEGFR labeled with VEGF-QDs during angiogenesis in ischemic legs.

Discussion

In vivo molecular imaging using high spatial precision in ischemic model mice is highly effective for the quantitative description of the molecular dynamics of VEGF and VEGFR during angiogenesis. This information can be applied to the development of treatments for ischemic disease. Previously described mouse models suffered from surgical limitations. These difficulties involved: (1) the induction of angiogenesis without arteriogenesis, an effect of arteries that remains after surgery; and (2) the induction of inflammation and edema during surgery.[10] We focused on the gastrocnemius, which is located deep in the thigh, and developed a new ischemic mouse model consisting of the ligation of 3 pairs of vessels: the superficial femoral, popliteal, and saphenous arteries and veins (Figure 1). We confirmed that angiogenesis was effectively induced in the model mice using conventional evaluation methods, histological capillary density measurements, and laser Doppler imaging (Figure 2D,K).

We have previously described the development of in vivo single-particle imaging using QDs with a spatial precision of 7-9 nm to clarify the molecular mechanisms of a anti-HER2 antibody-based drug delivery system and cancer metastasis in tumor-bearing mice.[8,9] In previous studies, in vivo imaging with high spatial precision was not applied to the visualization of angiogenesis. For this application in the current studies, we further modified our surgical fixation method (Figure 5). For the imaging technique used here, we designed a polyvinyl chloride plate with a window fit to the shape for the gastrocnemius. This window enabled us to observe the physiologic angiogenesis during active blood flow. We observed the in vivo molecular distribution of VEGF-QDs using this improved imaging in ischemic mice at 4, 9, and 14 days after a surgery in which angiogenesis in the gastrocnemius was effectively induced. The results demonstrate that a large number of VEGF-QDs specifically localized to the vessel wall in ischemic legs (Figure 6A-H), whereas fluorescence resulting from unconjugated QDs at the wall was very weak (supplemental Figure 2A-D). To quantitatively analyze the molecular distribution of VEGF-QD-labeled VEGFRs, we measured the total number of QDs
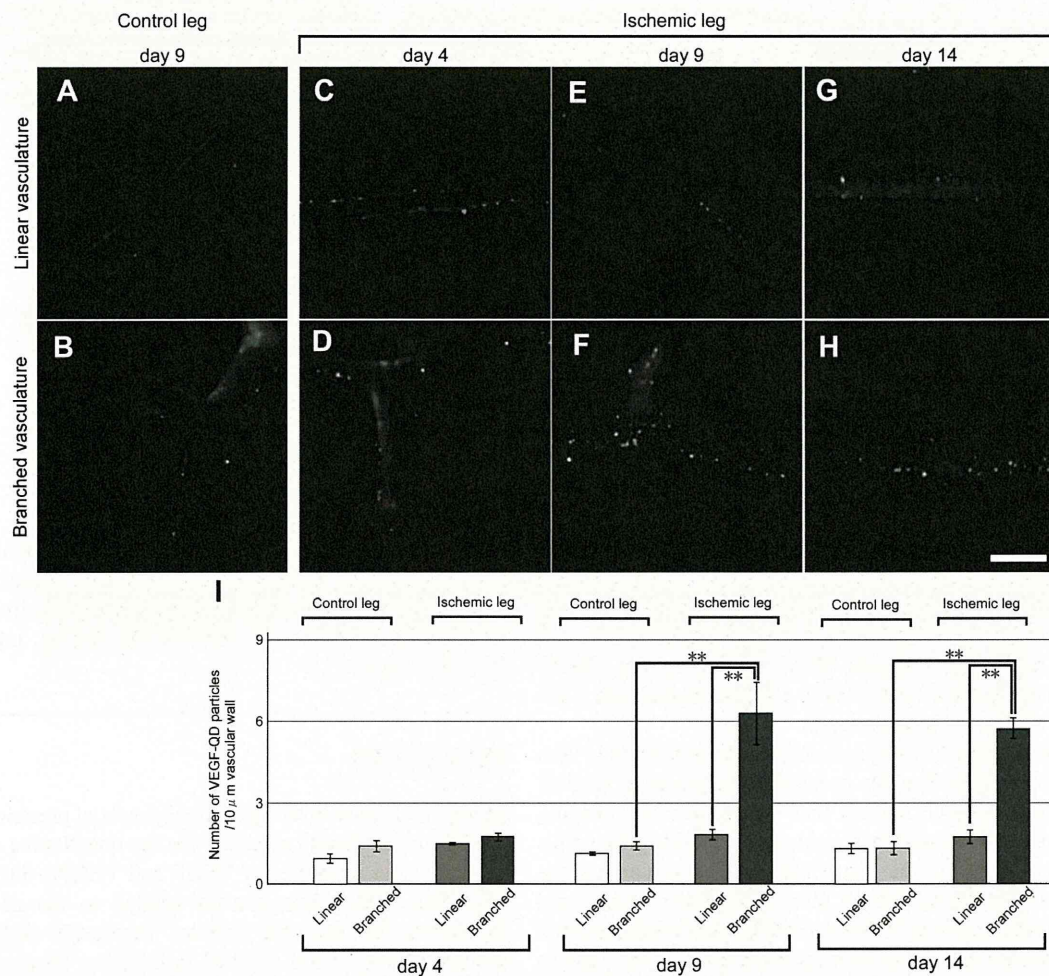
Figure 6. In vivo imaging of unconjugated and VEGF-QDs during angiogenesis in ischemic legs. (A-H) Typical images of vasculature in control and ischemic legs. These images were generated by overlaying 100 frames (200 ms/frame), each consisting of a 192-pixel square image, using Adobe after effect CS4 9.0.3 software. In model mice injected with VEGF-QDs, we observed "linear vasculature" (A,C,E,G) and "branched vasculature" (B,D,F,H) in control and ischemic mouse legs at 4, 9, and 14 days after operation. The data from unconjugated QDs are not shown (supplemental Figure 2). White dots represent QD fluorescence. Scale bar represents 10 μm. (I) The number of VEGF-QDs in different types of vasculature. The number of fluorescent particles per 10 μm of the vascular wall is quantified. n = 4. **$P < .05$. Error bars represent SEM.

(Figure 6I; supplemental Figure 2E). Because QDs with the same fluorescence wavelength are uniform in size, the fluorescence intensity of the QDs is proportional to the number of particles.[12] This property enabled us to determine relative VEGFR expression levels with a very high degree of accuracy. In mice 4 days after operation, there were no significant differences between the branched vasculature and the linear vasculature (Figure 6C-D,I). Furthermore, the IVIS Spectrum data from this time point did not show a significant difference in the accumulation of unconjugated QDs or VEGF-QDs in ischemic legs (Figure 4E). These data indicate that any VEGFR redistribution induced by hypoxic stimulation in ischemic legs occurs only at low levels at this time point. In mice at 9 days after operation, the data demonstrate a 3.4-fold greater number of VEGF-QDs on the walls of branched vasculature in ischemic legs than on the walls of linear vasculature in these legs and a 4.5-fold greater number than on the branched vasculature of control legs in model mice (Figure 6I). In mice at 14 days after operation, the data revealed that the number of VEGF-QDs on the walls of branched vasculature in ischemic legs was 3.3-fold greater than that on the linear vasculature in ischemic legs and 4.3-fold greater number than the number of VEGF-QDs on the branched vasculature in control legs in model mice (Figure 6I). These results demonstrate that the data acquired from mice at 9 and 14 days after operation using the single-particle

imaging technique were similar to data acquired using the IVIS Spectrum system (Figure 4F-G). From the data, it appears that the VEGFR protein expression on the branched vasculature in ischemic legs increases gradually between day 4 and day 9 via hypoxic stimulation, peaks at approximately day 9, and remains steady from day 9 to day 14. Histologic capillary density data reveal that capillary densities in ischemic legs increase gradually over 14 days (Figure 2D). It is very interesting, therefore, that the peak of VEGFR expression occurred ~ 9 days after the procedure. Furthermore, these data suggest that only a several-fold increase in the expression level of VEGFR on endothelial cells is critical for angiogenesis in ischemic tissues.

During angiogenesis, tip cells, stalk cells, and phalanx cells control vessel sprouting. Tip cells are located at the forefront of the sprouting vessel, stalk cells are located behind the tip cell at the branch, and phalanx cells are found in the unbranched endothelial layer.[13] Previous ex vivo studies reported that VEGFR expression in the tip cell is high to sense the VEGF concentration gradient in the extravascular area. In stalk cells, which control elongation of a new branch, VEGFR levels are lower than in the tip cells.[14] In phalanx cells, which normalize the endothelial cell layer, VEGFR levels are lower than in the stalk cells.[13] However, these are

qualitative data, and a quantitative analysis of the VEGFR distribution required to regulate the behavior of these cells has not been carried out in vivo. In addition, previous ex vivo data revealed that the amount of VEGFR protein involved in angiogenesis in ischemic tissue is 13-fold greater than in normal tissues.[15] In this report, however, because the total amount of VEGFR in both the vessel wall and the extravascular area was measured, the detailed quantitative distribution of VEGFR was not known. Our results suggest that only an approximately 3-fold difference in VEGFR distribution on the vascular wall is involved in the formation of branched vasculature from linear vasculature during angiogenesis (Figure 6I). The increase in VEGFR levels we observe after ischemia may quantitatively reveal a gradient of VEGFR expression levels between the stalk cells and pharynx cells.

Our results indicate that VEGFR distribution in in vivo ischemic tissues increased gradually over a specific period and remained steady at an approximately 3-fold increase. To increase the number of sprouting vessels for the operation of ischemic hypoxia, the steady several-fold increase of VEGFR expression levels at the ischemic site may be effective for controlled angiogenesis. Previously, treatment against ischemic hypoxia using VEGF gene therapy induced only a slight increase in VEGF blood concentrations.[16] In addition, overexpression of VEGF produces abnormal vessels in tumor angiogenesis.[17] These results suggest that in the context of ischemia, it is difficult to site-specifically modulate the concentration of a VEGF-related therapeutic to an appropriate value. Therefore, next-generation therapies targeting VEGFR, in addition to VEGF, may effectively induce site-specific angiogenesis for the treatment of ischemic disease. The novel in vivo imaging technique described here for the analysis of ischemic model mice may increase the understanding of the mechanisms of angiogenesis and aid in the development of VEGFR-related therapies.

Authorship

Contribution: Y.H. and K.G. designed and performed the research, analyzed the data, and wrote the manuscript; M.T., A.S., and N.O. performed research and analyzed data; M.W. and S.S. performed research; and T.Y. provided the equipment for laser Doppler perfusion imaging and performed research.

Conflict-of-interest disclosure: K.G. and M.T. have received a research grant from Konica Minolta Medical & Graphic Inc. N.O. has received research grants from Takeda Pharmaceutical Company Limited and Konica Minolta Medical & Graphic Inc. The remaining authors declare no competing financial interests.

Correspondence: Kohsuke Gonda, Department of Nano-Medical Science, Graduate School of Medicine, Tohoku University, Seiryo-machi, Aoba-ku, Sendai 980-8575, Japan; e-mail: gonda@med.tohoku.ac.jp.

References

1. Simons M. Angiogenesis: where do we stand now? *Circulation.* 2005;111(12):1556-1566.

2. Carmeliet P. Angiogenesis in life, disease and medicine. *Nature.* 2005;438(7070):932-936.

3. Helisch A, Schaper W. Arteriogenesis: the development and growth of collateral arteries. *Microcirculation.* 2003;10(1):83-97.

4. Simons M, Ware JA. Therapeutic angiogenesis in cardiovascular disease. *Nat Rev Drug Discov.* 2003;2(11):863-871.

5. Gowdak LHW, Poliakova L, Wang XT, et al. Adenovirus-mediated VEGF(121) gene transfer stimulates angiogenesis in normoperfused skeletal muscle and preserves tissue perfusion after induction of ischemia. *Circulation.* 2000;102(5):565-571.

6. Lu YX, Shansky J, Del Tatto M, Ferland P, Wang XY, Vandenburgh H. Recombinant vascular endothelial growth factor secreted from tissue-engineered bioartificial muscles promotes localized angiogenesis. *Circulation.* 2001;104(5):594-599.

7. Sakr Y. Techniques to assess tissue oxygenation in the clinical setting. *Transfus Apher Sci.* 2010; 43(1):79-94.

8. Gonda K, Watanabe TM, Ohuchi N, Higuchi H. In vivo nano-imaging of membrane dynamics in metastatic tumor cells using quantum dots. *J Biol Chem.* 2010;285(4):2750-2757.

9. Tada H, Higuchi H, Wanatabe TM, Ohuchi N. In vivo real-time tracking of single quantum dots conjugated with monoclonal anti-HER2 antibody in tumors of mice. *Cancer Res.* 2007;67(3):1138-1144.

10. Couffinhal T, Silver M, Zheng LP, Kearney M, Witzenbichler B, Isner JM. Mouse model of angiogenesis. *Am J Pathol.* 1998;152(6):1667-1679.

11. Limbourg A, Korff T, Napp LC, Schaper W, Drexler H, Limbourg FP. Evaluation of postnatal arteriogenesis and angiogenesis in a mouse model of hind-limb ischemia. *Nat Protoc.* 2009;4(12):1737-1748.

12. Hikage M, Gonda K, Takeda M, et al. Nano-imaging of the lymph network structure with quantum dots. *Nanotechnology.* 2010;21:18.

13. Carmeliet P, De Smet F, Loges S, Mazzone M. Branching morphogenesis and antiangiogenesis candidates: tip cells lead the way. *Nat Rev Clin Oncol.* 2009;6(6):315-326.

14. Gerhardt H, Golding M, Fruttiger M, et al. VEGF guides angiogenic sprouting utilizing endothelial tip cell filopodia. *J Cell Biol.* 2003;161(6):1163-1177.

15. Lu EX, Wagner WR, Schellenberger U, et al. Targeted in vivo labeling of receptors for vascular endothelial growth factor: approach to identification of ischemic tissue. *Circulation.* 2003;108(1):97-103.

16. Tongers J, Roncalli JG, Losordo DW. Therapeutic angiogenesis for critical limb ischemia: microvascular therapies coming of age. *Circulation.* 2008; 118(1):9-16.

17. Jain RK. Normalization of tumor vasculature: an emerging concept in antiangiogenic therapy. *Science.* 2005;307(5706):58-62.

Methods for Assessment of Effects of Habitual Exercise on the Autonomic Nervous Function Using Plethysmogram

Makoto Yoshizawa, *Member, IEEE*, Norihiro Sugita, Tomoyuki Yambe, *Member, IEEE*, Satoshi Konno,
Telma Keiko Sugai, *Student Member, IEEE*, Makoto Abe, Noriyasu Homma, *Member, IEEE*

Abstract—The present paper has proposed two methods for obtaining the linear correlation of the baroreflex system without measurement of blood pressure. One is based on the pulse wave transit time which needs both the electrocardiogram and the photoplethysmogram. The other is based on the photoplethysmogram only. The results from the experiments showed that the effect of habitual exercise and the Valsalva maneuver can be verified quantitatively. The proposed methods are possible to be used for a test of the autonomic nervous function at home.

I. INTRODUCTION

JAPAN is being a super-aging society, and thus the inflation of nationwide medical cost can be predicted exactly in the very near future. To prevent the crisis in the nation's deficit-ridden health insurance system, we should seriously consider some strategies for protecting people's health.

In this situation, one of the most effective methods is to entrench people to exercise habitually, which may be valid especially for people suffering from metabolic syndrome instructed to the specific medical checkup. To promote habitual exercise, some indices representing the effect of exercise should be fedback to the person after the exercise.

It has been indicated that the index corresponding to linear correlation of the baroreflex system is useful for expressing the autonomic nervous function [1,2]. We adopted this index as information fedback to the person exercising to settle it a habit.

Unfortunately this index needs measurement of continuous blood pressure to calculate. However it is not easy to measure continuous blood pressure because its sensor is too expensive and bulky to use at an ordinary home.

In this article, two alternative methods without measuring continuous blood pressure are introduced. One is a method in which the pulse wave transit time (PTT [ms]) is used

instead of continuous blood pressure, and PTT is obtained from electrical cardiogram (ECG) and photoplethysmogram (PPG). The ECG is also difficult to measure at home and should not be used if possible. The other method does not need the ECG signal but linear correlation can be still obtained on the basis of only PPG signal.

In the use of these methods, the effect of habitual exercise on the index was evaluated and Valsalva maneuver was employed to ascertain the capability of the proposed method to extract individual difference from the calculated index.

II. METHODS

A. Method Based on Pulse Wave Transit Time

Monitoring device

For home use, a measurement device should be wireless with less constraint. There are many monitoring systems but RF-ECG (Micro Medical Device, Inc.) is unique as a very small (40mm×35mm×7.4mm) and light (11.8g including electrical cell) wireless monitoring sensor to measure not only ECG but also acceleration and temperature as shown in Fig.1a).
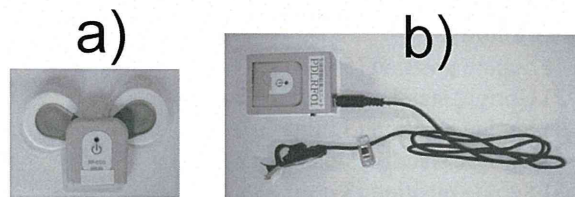

Fig. 1 Wireless sensors for measuring a) ECG signal and b) photo-plethysmographic signal

However, there is no small sized wireless device which can measure both ECG and PPG signals. In this study, we developed a sensor based on RF-ECG whose input terminal can acquire the PPG signal by attenuating its voltage level as shown in Fig.1b). To avoid the effect of body motion, the PPG signal was measured at the ear lobe and the sensor itself was inserted into a pocket on the chest of the subject's cloth. Another RF-ECG was used simultaneously to measure the ECG signal. Thus, both ECG and PPG signals can be measured in a wireless fashion at the sampling rate of 204Hz with less restriction.

The heart rate HR [bpm] was obtained from the reciprocal of the ECG signal, and PTT was calculated as the interval from the peak time of R-wave of the ECG signal

1157

to the peak time of the velocity of the PPG signal. Both PTT and HR were band-pass filtered with a pass band between 0.08Hz and 0.12Hz to be limited to the Mayer wave-related frequency components. After the processing, cross-correlation coefficient $\rho(\tau)$ between these signals was calculated time-discretely as follows:

$$\rho(\tau) = \frac{\phi_{PTT,HR}(\tau)}{\sqrt{\phi_{PTT,PTT}(0) \cdot \phi_{HR,HR}(0)}} \qquad (1)$$

where $\phi_{PTT,HR}(\tau)$ is the cross-correlation function between PTT and HR, and $\phi_{PTT,PTT}(\tau)$ and $\phi_{HR,HR}(\tau)$ are auto-correlation functions of PTT and HR, respectively. In this study, $\rho(3)$, i.e., the value of $\rho(\tau)$ at $\tau = 3$ s was obtained as an index which represents the linear correlation of the baroreflex system from PTT to HR. The index $\rho(3)$ is more stable value than the conventional index ρ_{max} which is defined as the maximum value of $\rho(\tau)$ in spite of its lower value.

Experiment
In the experiment, elderly people were used as test subjects classified into two groups. One is the Exercise Group consisting of 8 healthy people (age 52 to 73; mean 65.6±7.7; 4 males and 4 females) exercising habitually for over 15min a week. The other is the Control Group consisting of 8 almost healthy people (age 55 to 75; mean 67.6±6.5; 3 males and 5 females) exercising little

To give dynamic change in subject's hemodynamics by using change in his or her posture, the experimental protocol was as follows:
1) Supine position (5 min)
2) Upright standing position (2 min)
3) Supine position (3 min)
4) Upright standing position (2 min)
5) Supine position (3 min)

B. . Method Based Only on Photoplethysmogram

Estimation of cross-correlation function
So far, many methods for obtaining blood pressure based on photoplethysmogram have been proposed, in which, for example, local maximum or minimum values of the acceleration of the signal are utilized. The purpose of these methods is usually to obtain the absolute value of blood pressure. However, if the purpose is to estimate the linear correlation of the baroreflex system, we can do it as shown below.

First, as shown in Fig.2, obtain the feature variables specifying the PPG signal at a certain beat such as the first extremum a and the second extremum b of the acceleration, the second extremum B of the velocity, the mean value MP and the difference PA between the maximum and minimum values of the signal within the beat. Since these variables are sampled every unequally-spaced interval,

resample it every equally-spaced interval of 0.2s (5Hz) after the cubic spline interpolation. Let k be a discrete time which is incremented with the resampling, and produce a feature vector given by

$$x(k) = [a, b, b/a, a^2, b^2, ab, B/a, MP, PA]^T \qquad (2)$$

Consider a multiple regression model in which an explanatory variable is $x(k)$ and an objective variable is heart rate $y(k)$ as follows:

$$\hat{y}(k) = \beta^T x(k) + \varepsilon(k) \qquad (3)$$

where β is a coefficient vector to be identified with the least square method and $\varepsilon(k)$ is a residue. In general, it is expected that cross-correlation between blood pressure and heart rate whose frequency components are limited to the Mayer wave-related band is maximized a few second later. This phenomenon means that the baroreflex system has a delay. Let denote the delay as L [ms]. Unfortunately, the value of L is changed with time and subjects. Thus, find the optimal values β^* and L^* corresponding to β and L, respectively, so that the error between the $\hat{y}(k)$ and $y(k)$ can be minimized.

Instead of the value of (1), calculate a surrogate value that is obtained by letting $PTT = \hat{y}(k)$ and $HR = y(k)$ in (1). In this case, heart rate $HR = y(k)$ is calculated from the foot-to-foot interval (FFI [ms]) of the PPG.
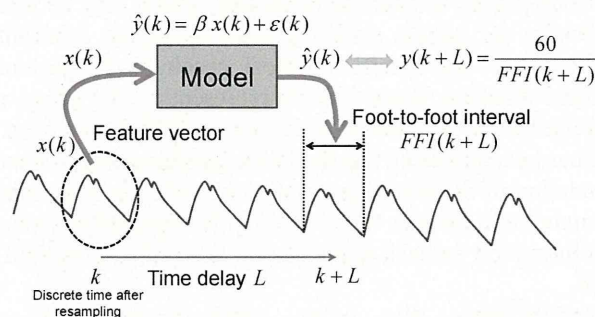

Fig.2 Multiple regression model with the input feature vector of pulse wave for estimation of heart rate.

The reason why the cross-correlation between heart rate and its estimate can be substituted by that between blood pressure and heart rate is shown below. It is known that heart rate correlates closely with blood pressure in the Mayer wave-rerated band at a resting state. If the output of the multiple regression model agrees well with the actual blood pressure, it is likely that the estimate obtained from the model also correlates well with heart rate.

On the other hand, the other method for estimation of blood pressure based on the PPG needs same calibration process using a blood pressure sensor. However, the proposed method employs the subject's heart rate as a reference value to identify the model parameters and does not needs any blood pressure sensor. While the method described in 2.1 which uses the PTT requires the ECG sensor

1158

to specify the position of the R-wave, the proposed method uses only the PPG sensor which is cheap and expected to be widely spread.

Estimation of cross-correlation function

Thirty-two healthy subjects (Age 23.1±3.6; 24 males; 8 females) were used in an experiment including the Valsalva maneuver with a protocol as follows:

1) Rest (5 min)
2) Respiration cease (1 min)
3) Rest (3 min)
4) Respiration cease (1 min)
5) Rest (5 min)

A photo sensor and an amplifier for (BIOPAC; PPG100C) was used to measure the PPG signal at the index finger and blood pressure sensor (Finapres; Portapres) was used to measure continuous blood pressure at the middle finger.

III. . RESULTS AND DISCUSSION

A. . Method Based on Pulse Wave Transit Time

Figure 3 shows a subject's data (Age 70; female; systolic/diastolic pressure=136mmHg/84mmHg) who was a member of the Exercise Group. The data are time courses of heart rate, HR, the normalized PTT to have zero mean and unit standard deviation, and the cross-correlation coefficient at $\tau = 3$, $\rho(3)$. At two parts of the upright standing position, HR increased like a rectangular shape, which corresponds to normal orthostatic baroreflex to regulate blood pressure. It is found that PTT also increased in the similar manner as HR but their shapes are not so similar. Decrease in $\rho(3)$ can be seen at the two parts around upright standing positions.

Figure 4 shows another subject's data (Age 72; female; systolic / diastolic pressure= 155mmHg / 102mmHg) who was a member of the Control Group. Unlike Fig.4, hear rate HR changed irregularly, which means the baroreflex did not work well. Moreover, the shape of PTT is very similar to that of HR. This fact may be caused by arterial sclerosis since she had light hypertension and she was taking depressor drug routinely. That is to say, the change in HR may be equal to that of PTT if blood vessel is like a lead pipe with less compliance. The absolute value of $\rho(3)$ was small and drifted around zero during the experiment, which implies that the regulation function manipulating HR based on blood pressure with 3 seconds delay was not well done by the autonomic nervous system.
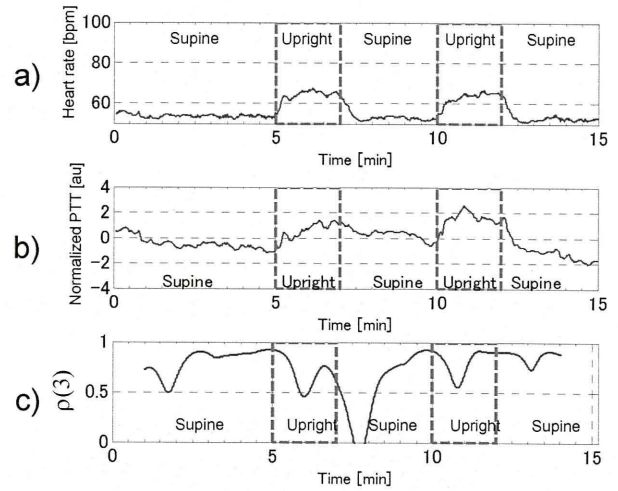

Fig.3   a)heart rate, b)normalized PTT and c)cross-correlation function $\rho(3)$ of a subject belonging to the Exercise Group (female; age 70; Systolic / diastolic pressure = 136mmHg/84mmHg).

Figure 5 shows the comparison of the mean value $\rho(3)$ between the Exercise and the Control Groups. It is found that the recovery speed of $\rho(3)$ of the Control Group was significantly lower than that of the Exercise Group in the interval between two upright standing positions. It can be guessed that this difference was caused by the effect of habitual exercise.
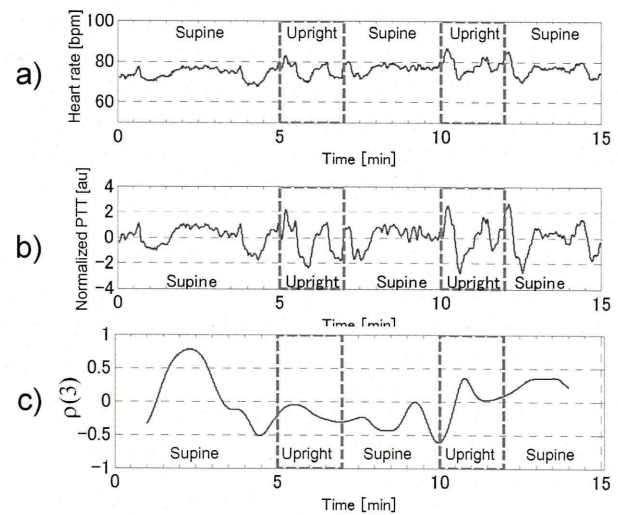

Fig.4   a)heart rate, b)normalized PTT and c)cross-correlation function $\rho(3)$ of another subject belonging to the Control Group (female; age 72; Systolic / diastolic pressure = 155mmHg /102mmHg).
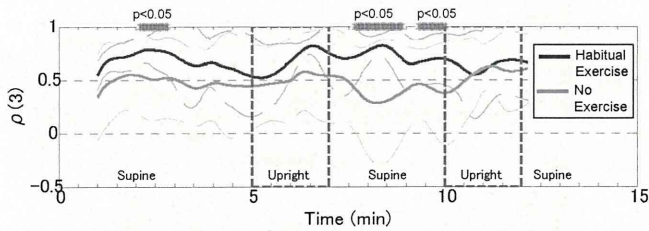
1159

Fig.5 Comparison of $\rho(3)$ between the Exercise Group (n=8) and the Control Group (n=8). Solid line: mean. Broken line: S.D.

B. . Method Based Only on Photoplethysmogram

The mean value of thirty-two subjects' $\rho(3)$ obtained from the method based only on the PPG signal described in 2.2 are shown in Fig.6, accompanied by $\rho(3)$ calculated directly from measured blood pressure. The figure indicates that $\rho(3)$ based on the PPG is much lower than $\rho(3)$ based on the blood pressure and that the effect of respiration cease on the time trajectories was not clear in both two kinds of $\rho(3)$ s. The reason is that the data shown in Fig.6 includes the subjects whose $\rho(3)$ is low even in the resting state. It can be guessed that such subjects tend to have a dull autonomic nervous reflex function against the respiration cease.

Thus, the subjects were selected under the condition that the mean value of $\rho(3)$ in the resting state from 0min to 4min was higher than 0.5. There were 9 subjects who satisfy the condition, and the mean value of $\rho(3)$ of these subjects is shown in Fig.7. It seems that the decrease in $\rho(3)$ around the positions of the respiration cease got deep.

In the same way, when the threshold to select the subjects was increased to 0.7, four subjects survived and their mean value of $\rho(3)$ was shown in Fig.8. It can be found that the depth of the decrease around the respiration cease tended to get deeper and that the value of $\rho(3)$ based on the PPG in the resting state came closer to that based on the blood pressure.

These results suggest that the temporal change in the linear correlation of the baroreflex system can be estimated on the basis of the PPG signal only without measurement of the ECG or blood pressure. Moreover, it is possible that $\rho(3)$ based on the PPG is more sensitive to the effect of the respiration cease than $\rho(3)$ based on blood pressure.
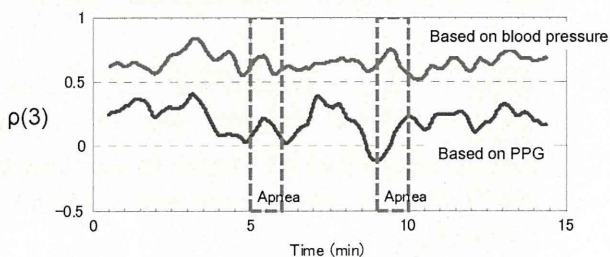

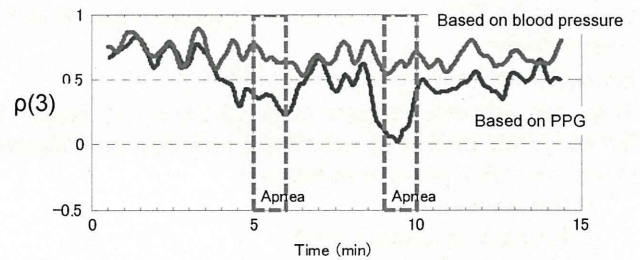Fig. 6 Mean value of $\rho(3)$ over all 32 subjects.

Fig.7 Mean value of $\rho(3)$ over 9 subjects whose mean value is larger than 0.5 from 0min to 4min.
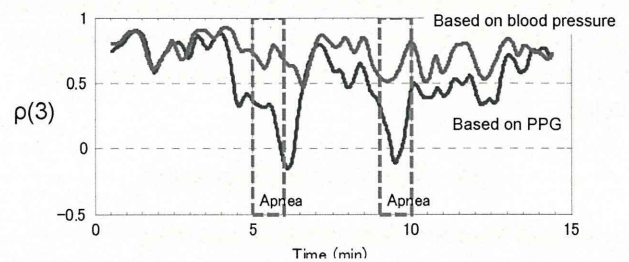

Fig.8 Mean value of $\rho(3)$ over 4 subjects whose mean value is larger than 0.7 from 0min to 4min.

IV. CONCLUSIONS

The present study has developed two methods for obtaining the linear correlation of the baroreflex system without measurement of blood pressure. One is based on the pulse wave transit time which needs both the ECG signal and the photoplethysmogram. The other is based on the photoplethysmogram only. The results from the experiment with the former method showed that the effect of habitual exercise can be verified quantitatively. The latter method indicated that the response of the linear correlation to the Valsalva maneuver can be estimated. The proposed methods are possible to be used for a test of the autonomic nervous function easily even at home.

REFERENCES

[1] Yoshizawa M, Sugita N, Tanaka A, Abe K, Yambe T, Nitta S: Quantitative and physiological evaluation of three dimensional images. Proceeding of the 7th International Conference on Virtual Systems and Multimedia: pp. 864-871, 2001

[2] Sugita N, Yoshizawa M, Abe M, et al: Evaluation of adaptation to visually induced motion sickness based on the maximum cross-correlation between pulse transmission time and heart rate, Journal of NeuroEngineering and Rehabilitation, vol. 4, no. 35, (Online Journal), 2007 (http:// www. jneuroengrehab. com/ content/ pdf/ 1743-0003-4-35.pdf)

1160

Numerical Analysis of Effects of Measurement Errors on Ultrasonic-Measurement-Integrated Simulation

Kenichi Funamoto*, Toshiyuki Hayase, Yoshifumi Saijo, and Tomoyuki Yambe

Abstract—Ultrasonic-measurement-integrated (UMI) simulation, in which feedback signals are applied to the governing equations based on errors between ultrasonic measurement and numerical simulation, has been investigated for reproduction of the blood flow field. However, ultrasonic measurement data inherently include some errors. In this study, the effects of four major measurement errors, namely, errors due to Gaussian noise, aliasing, wall filter, and lack of data, on UMI simulation were examined by a numerical experiment dealing with the blood flow field in the descending aorta with an aneurysm, the same as in our previous study. While solving the governing equations in UMI simulation, Gaussian noise did not prevent the UMI simulation from effectively reproducing the blood flow field. In contrast, aliasing caused significant errors in UMI simulation. Effects of wall filter and lack of data appeared in diastole and in the whole period, respectively. By detecting significantly large feedback signals as a sign of aliasing and by not adding feedback signals where measured Doppler velocities were aliasing or zero, the computational accuracy substantially improved, alleviating the effects of measurement errors. Through these considerations, UMI simulation can provide accurate and detailed information on hemodynamics with suppression of four major measurement errors.

Index Terms—Biofluid mechanics, computational fluid dynamics, measurement-integrated (MI) simulation, ultrasonic devices.

I. INTRODUCTION

STRESSES due to blood flow on a blood vessel wall (hemodynamic stresses) are closely related to development and progression of circulatory diseases such as atherosclerosis and aneurysms. The results of *in vitro* cellular experiments [1], [2], animal experiments [3], [4], numerical simulations of blood flow [5], and comparison of those results with clinical findings [6], [7] have indicated the mechanisms of circulatory diseases. Especially, changes of state of endothelial cells by wall

shear stress (WSS) have been intensively investigated, and some relationships between circulatory diseases and WSS have been proposed. For instance, low, oscillatory WSS causes atherosclerosis, and a bifurcation of an artery such as a carotid artery is well known as a likely site of atherosclerosis [8]. Concerning aneurysms, though there are conflicting suggestions that low/high WSS may lead to the ruptures [6], [7], WSS of physiologically abnormal magnitude is a possible trigger.

Among methods to measure blood flow field, ultrasonic measurement is characterized by noninvasive, real-time visualization of hemodynamics as well as blood vessel configuration by means of color Doppler imaging. In this method, pulses of ultrasound are transmitted from an ultrasound probe along scanning lines on a plane at a certain pulse repetition frequency (PRF), or a sampling frequency, and the echo from tissue is received with the same probe. Then, the magnitudes of the echo signals along the scanning lines are converted to brightness to visualize the tissue configuration, and the Doppler velocity is calculated from the Doppler shift frequency of the echo signal. Note that the Doppler velocity is the one-directional component of the velocity vectors along the ultrasonic beam, and practice and time are required to recognize the 3-D complicated hemodynamics. Moreover, hemodynamic stresses of WSS and pressure cannot be directly obtained with this method. On the other hand, numerical simulation of blood flow provides information on hemodynamic stresses as well as on the blood flow field [5]. Recently, fluid–structure interaction simulation enables investigation of the blood flow field considering the blood vessel wall motion due to its elasticity [9]. Numerical simulation essentially depends on boundary and initial conditions. However, it is difficult to precisely set these conditions in the numerical simulation of *in vivo* complicated unsteady blood flow [10], resulting in a computational result which may be different from the real blood flow.

Measurement-integrated (MI) simulation or a flow observer, which integrates measurement and numerical simulation, has been investigated as a methodology to overcome individual limitations in measurement and computation. Hayase and Hayashi [11] conducted a numerical experiment, showing that turbulent flow in a square duct was reproduced by MI simulation. Nisugi *et al.* [12] developed a hybrid wind tunnel, which integrated experimental wind tunnel measurement and numerical simulation, and analyzed a Karman vortex street behind a square cylinder. In addition, Yamagata *et al.* [13] performed MI simulation of the Karman vortex street with particle image velocimetry (PIV) measurement. Nakao *et al.* [14] fed back measurement data on velocity and pressure in an orifice to a numerical simulation with a k–ε turbulent model and achieved improvement of computational accuracy.
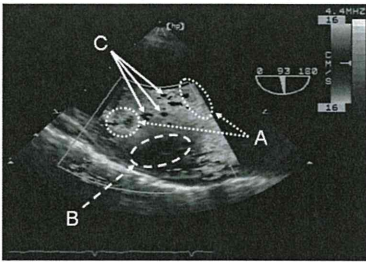
Fig. 1.   Example of color Doppler imaging of a thoracic aneurysm in systole with indications of measurement errors. (A) Aliasing, (B) wall filter, and (C) lack of data.

As medical applications of MI simulation, the authors have proposed integration of medical measurement (ultrasonic measurement or MRI) of blood flow velocity and a numerical simulation to reproduce the blood flow field [15]–[17]. Ultrasonic-MI (UMI) simulation feeds back errors between measured and computed Doppler velocities to the numerical simulation to make the computational result converge to the real flow [16]. In our previous numerical experiments [15], [16], the efficiency of the UMI simulation was revealed, and the transient and steady characteristics of the method were investigated. In these studies, unsteady or steady numerical solution with realistic boundary conditions was first defined as the standard solution. Then, UMI simulation with inaccurate boundary conditions but with the same flow volume was evaluated as to how it reproduced the standard solution. In the feedback process, for purposes of simplicity, Doppler velocities of the standard solution were used without consideration of measurement errors.

Ultrasonic measurement of real *in vivo* blood flow inherently includes some measurement errors. Fig. 1 shows an example of a color Doppler image of an aneurysm in the descending aorta by means of transesophageal ultrasonography [18]. Noise is a cause of measurement error, adding some deviance to the Doppler velocity. Moreover, the settings of ultrasound Doppler measurement may cause measurement errors. The range of measurable Doppler velocity is defined by the PRF in the ultrasound Doppler measurement. In case the Doppler shift frequency exceeds half of the PRF, it is regarded as a frequency shift from a frequency different from the true one, resulting in aliasing, by which the Doppler velocity with incorrect direction and magnitude in regions with high blood flow velocity is provided (see "A" in Fig. 1). Color Doppler imaging utilizes a wall filter or a moving target indicator (MTI) filter which ignores the components of the Doppler shift frequency less than a certain value to distinguish tissue motion and blood flow. This filtering is effective for extracting blood vessel configuration, but it incidentally provides zero velocity in regions with slow blood flow velocity in a blood vessel (see "B" in Fig. 1). Furthermore, measurement data may be lacking at measurement points when the intensity of echo signals from blood cells is too small or when artifacts occur (see "C" in Fig. 1).

Feedback using measurement data with the aforementioned measurement errors may lead to UMI simulation with computational results different from the real blood flow field. Hence, this study investigated the effects of four major measurement

TABLE I
CLASSIFICATION OF STANDARD SOLUTION (SS), ORDINARY SIMULATION (OS), AND UMI SIMULATION (UMIS)

Name	Inlet	Outlet	Feedback
SS	realistic velocity profile	realistic velocity profile	No
OS	uniform velocity profile	free flow	No
UMIS	uniform velocity profile	free flow	Yes

errors, i.e., errors due to noise (Gaussian noise), aliasing, wall filter, and lack of data, on the UMI simulation by a numerical experiment dealing with a 3-D unsteady blood flow field in a descending aorta with an aneurysm, the same as in our previous study [16]. The treatments for each measurement error are also discussed.

II. METHODS

It is difficult to obtain 3-D information on the blood flow field by measurement, though such information is indispensable to evaluate computational accuracy of UMI simulation. Consequently, effects of measurement errors on UMI simulation were investigated by applying the methods employed in our previous numerical experiment dealing with a 3-D unsteady blood flow field in an aneurysm [16]. A numerical solution of blood flow simulation obtained with realistic boundary conditions was first defined as the standard solution or a model of real flow, and the Doppler velocities corresponding to an ideal measurement data were obtained. For the Doppler velocities of the standard solution, one of four measurement errors due to Gaussian noise, aliasing, wall filter or lack of data was introduced. Assuming that the exact boundary conditions were unknown, a UMI simulation and an ordinary simulation were performed with inaccurate boundary conditions. For the UMI simulation, a feedback signal was applied using the Doppler velocity of the standard solutions with/without measurement errors. The computational accuracy of each UMI simulation was evaluated as to reproduction of the original standard solution, compared with that of an ordinary simulation without feedback. Table I summarizes the computational simulations conducted in this study.

A. UMI Simulation

Governing equations of UMI simulation of blood flow are the Navier–Stokes equations for incompressible and viscous fluid flow

$$\rho \left(\frac{\partial \mathbf{u}}{\partial t} + (\mathbf{u} \cdot \nabla) \mathbf{u} \right) = \mu \Delta \mathbf{u} - \nabla p + \mathbf{f} \qquad (1)$$

and the pressure equation

$$\Delta p = -\nabla \cdot \rho (\mathbf{u} \cdot \nabla) \mathbf{u} + \nabla \cdot \mathbf{f} \qquad (2)$$

where ρ and μ are, respectively, the density and viscosity of blood, t is time, $\mathbf{u} = (u, v, w)$ is the velocity vector, and p is the pressure. $\mathbf{f} = (f_x, f_y, f_z)$ denotes the artificial body force or the feedback signal which is applied at feedback points defined in a feedback domain. The pressure equation, (2), is derived by substituting the equation of continuity into the divergence of the Navier–Stokes equation, Eq. (1).
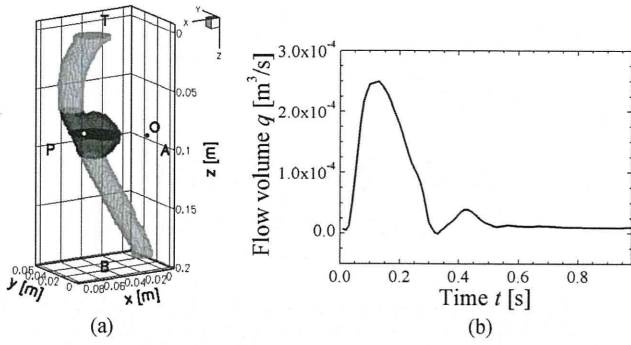
Fig. 2. (a) Computational domain with a feedback domain (gray zone), a probe position at O, and a monitoring point (white dot), and (b) variation of flow volume in one cardiac cycle.

The feedback signal in UMI simulation is defined as being proportional to the optimal estimation of the difference in velocity vector obtained by Doppler velocities by means of ultrasonic measurement and the numerical simulation

$$\mathbf{f} = -K_v^* \frac{\Phi_d \left(\mathbf{u}_c - \mathbf{u}_s \right)}{U} \left(\frac{\rho U^2}{L} \right) \tag{3}$$

where K_v^* is the feedback gain (nondimensional), U is the characteristic velocity, L is the characteristic length, $\mathbf{u}_c$ and $\mathbf{u}_s$ are velocity vectors of the computational result and the standard solution (or real flow), respectively, and Φ_d ($d = 1, 2, 3$) is a projection function of a 3-D vector to the d-dimensional subspace generated by the vectors of the ultrasonic beam directions. Note that the special case with $K_v^* = 0$ is an ordinary numerical simulation without feedback. The acquisition of Doppler velocity by projecting a velocity vector in the direction of the ultrasonic beam corresponds to the case of $d = 1$. In numerical simulation, all parameters are nondimensionalized by characteristic values. Reference length, L, and reference velocity, U, are the entrance diameter of the blood vessel, D, and mean inlet velocity at peak flow, $u'_{\max}$, respectively, and blood density ρ is used as the reference density. The above governing equations are discretized and solved by means of the finite volume method. Feedback signals are updated and added at each iteration step using the latest velocity results. For detailed descriptions of the projection function, Φ_d, and discretization, see our previous study [16].

B. Procedure of Numerical Experiment

Every setting to obtain the standard solution and to perform the UMI simulation was the same as that in the previous study [16]. Briefly, the objective was the blood flow in a chronic aortic aneurysm in the descending aorta in a 76-year-old female patient, who had no significant complications (see Fig. 2(a)). The configuration of the whole aorta from the ascending aorta to the abdominal aorta including the aneurysm was reconstructed by accumulating the X-ray CT images (AquilionTM 16, Toshiba, Tokyo, Japan) with commercial 3-D reconstruction software (Mimics 7.3, Materialise, Leuven, Belgium). All computations were performed in the computational domain shown in Fig. 2(a) with an original program similar to the SIMPLER method. In

the computational program, a consistently reformulated QUICK scheme was used for discretization of the convective terms in Navier–Stokes equations, and a second-order implicit scheme was employed for that of time derivative terms [16]. The computational grid consisted of an orthogonal equidistant staggered grid system with $43 \times 30 \times 91$ grid points in the x, y, and z directions, respectively. First, we performed a computation to obtain the standard solution by applying unsteady velocity profiles at the upstream and downstream boundaries. These boundary conditions were obtained from a preliminary simulation in the whole aorta, including the present domain by using commercial computational fluid dynamics software (FLUENT 6.1.22, Fluent, Inc., Lebanon, NH). This is because the orthogonal grid system of the present scheme is not efficient for the analysis of the whole aorta domain. Zero velocity was assumed on the wall. Seventy percent of the cardiac output of 7.0×10^{-5} m³/s (4.2 l/min) was assumed to flow through the blood vessel. The heart rate was 61 bpm (1.02 Hz), so that one cardiac cycle was $T^* = 0.98$ s. The variation of blood flow volume was provided with reference to [19], as shown in Fig. 2(b). The inlet diameter of the blood vessel, D ($=L$), was 29.25×10^{-3} m, and the mean inlet velocity at peak flow, $u'_{\max}$ ($=U$), was 36.70×10^{-2} m/s. Consequently, the reference time T ($=D/U$) was 7.97×10^{-2} s. The density and viscosity of blood were set at $\rho = 1.00 \times 10^3$ kg/m³ and $\mu = 4.00 \times 10^{-3}$ Pa·s, respectively, within the normal range. The computational time step sufficient to obtain an accurate result was $\Delta t = 0.01$ s (0.125, nondimensionally) as shown by test computations.

A former study dealing with reproduction of 3-D steady flow revealed that the positioning of an ultrasound probe affected the computational result of the UMI simulation, and that using such a probe at the same height of an aneurysm yields the best reduction of the error in the velocity field in the aneurysmal domain and a fast response to the targeted steady state of the blood flow field [15]. Hence, in the UMI simulation, one probe was located at the point O [$(x, y, z) = (0.49, 0.00, 2.94)$ ((0.014 m, 0.000 m, 0.086 m), dimensionally)] in Fig. 2(a) for the acquisition of Doppler velocities at all the grid points in the fluid region of domain M [$2.26 \leq z \leq 3.62$ (0.066 m $\leq z \leq 0.106$ m, dimensionally), shown by dark gray in Fig. 2(a)], which covered the whole aneurysmal domain, including the parent blood vessel. To obtain information on Doppler velocities in domain M, transesophageal ultrasonography with rotation of the beam plane was assumed. Regarding the boundary conditions, the exact boundary conditions for the standard solution were assumed to be unknown, and the UMI simulation was carried out with simple boundary conditions: zero velocity on the wall, an unsteady parallel flow with a uniform velocity profile at the inlet, and a free flow condition ($\partial/\partial n = 0$, n: coordinate normal to the boundary) at the outlet with the same flow volume as the standard solution in Fig. 2(b) (see Table I). Concerning the initial condition, UMI simulation in this study started from a zero velocity field. Though the inaccurate boundary conditions introduced error to the blood flow field in the aneurysm, the addition of feedback signals at the feedback points worked to reduce the error in the UMI simulation.

C. Introduction of Measurement Error

In order to evaluate the effects of measurement errors on the UMI simulation, Doppler velocities of the standard solution with one of four measurement errors of noise, aliasing, wall filter, and lack of data were individually used for feedback. For the introduction of the measurement error, a measurable Doppler velocity range, which was determined by the PRF in ultrasound Doppler measurement, was referred to. Generally, for color Doppler imaging of blood flow in the descending aorta by transesophageal ultrasonography, the Doppler velocity range (see a color bar in Fig. 1) is set to be relatively small since targeted blood flow is close to an ultrasound probe (see a probe position O in Fig. 2(a)). The typical measurable Doppler velocity range, $|V_0|$, for color Doppler imaging of the standard solution was thought to be within $|V_0| < 0.87$ (32 cm/s, dimensionally), referring to the incidence degrees of aliasing described later. The setting of a transesophageal ultrasound probe corresponds to a PRF of 3.7 kHz and a center frequency of 4.4 MHz [18]. Since it is difficult to specify the amounts of measurement errors, they were set in appropriate ranges.

1) Gaussian Noise: Doppler velocity can be different from the true value due to the effect of noise; ultrasound measurement provides Doppler velocity as a summation of the true value and some deviance

$$V' = V + \tilde{V}. \tag{4}$$

In this study, noise, assumed to follow the normal distribution $N(\mu_V, \sigma_V{}^2)$ with $\mu_V = 0$ and with four different values of the standard deviation, $\sigma_V = 0.011$, 0.022, 0.044, and 0.087 (0.4, 0.8, 1.6, and 3.2 cm/s, dimensionally), was respectively added to the Doppler velocity of the standard solution. For the sake of simplicity, the occurrence of aliasing was not considered in the process. Note that idealized ultrasonic measurement without noise corresponds to the case of $\sigma_V = 0$. The above settings were equivalent to the cases that deviances due to noise were 1.25%, 2.5%, 5%, and 10% values against the magnitude of the typical measurable Doppler velocity range of $|V_0| = 0.87$ (32 cm/s, dimensionally). For instance, variations of Doppler velocity of the standard solution at a monitoring point $[(x, y, z) = (1.84, 1.16, 2.94), ((0.054 \text{ m}, 0.034 \text{ m}, 0.086 \text{ m}), \text{dimensionally}), a white dot in Fig. 2(a)]$ in the parent artery in one cardiac cycle in the cases of $\sigma_V = 0$, 0.022, and 0.087 are shown in Fig. 3. With increasing standard deviation, σ_V, deviance against the ideal ultrasonic measurement data ($\sigma_V = 0$) or the true Doppler velocity increases at each time moment. The effect of noise is relatively significant in diastole ($t/T^* > 0.4$) when the blood flow velocity itself is low.

2) Aliasing: PRF determines the range of measurable Doppler velocity. Doppler velocity whose magnitude exceeds that of the measurable Doppler velocity is folded and is recognized as velocity with incorrect magnitude and direction (see "A" in Fig. 1). Specifically, if the magnitude of Doppler velocity, V, exceeds that of the measurable Doppler velocity, V_{thre}, V is provided as V' which is within $\pm|V_{\text{thre}}|$ with the following
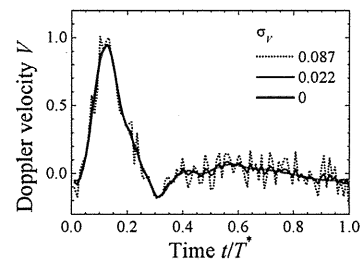

Fig. 3.   Doppler velocity at a grid point, $(x, y, z) = (1.84, 1.16, 2.94)$ ((0.054 m, 0.034 m, 0.086 m) in dimensional values), with Gaussian noise with three different degrees of standard deviation, σ_V, in one cardiac cycle (nondimensional).

transformation:

$$V' = \begin{cases} 2|V_{\text{thre}}| + V & (V < -|V_{\text{thre}}|) \\ V & (|V| < |V_{\text{thre}}|) \\ -2|V_{\text{thre}}| + V & (|V_{\text{thre}}| < V). \end{cases} \tag{5}$$

In this study, the threshold value, $|V_{\text{thre}}|$, of measurable Doppler velocity was set at four different values of 0.22, 0.44, 0.87, or 1.09 (8, 16, 32, or 40 cm/s, dimensionally). Among them, color Doppler images with $|V_{\text{thre}}| = 0.87$ well visualized both small and large Doppler velocities in the aneurysm in the cardiac cycle though some aliasing occurred. Hence, the setting of the threshold of Doppler velocity was considered as the normal setting, $|V_0|$. The percentage of points where aliasing occurred in the feedback points, N_A/N_{FB}, at each time step is shown in Fig. 4(a). With decreasing measurable Doppler velocity range, aliased points increased. The timing of the maximum value of N_A/N_{FB} does not necessarily coincide with that of the maximum flow rate due to the relationship between an ultrasound beam angle and the vortex in the aneurysm ($t/T^* = 0.13$; see Fig. 2(a)).

3) Wall Filter: Generally, color Doppler imaging utilizes a wall filter, called an MTI filter, to distinguish blood flow and blood vessel wall motion. The filter enables the extraction of blood flow, but it tends to display slow Doppler velocities as zero near the blood vessel wall, in an aneurysm and at locations where blood flow direction is approximately perpendicular to the ultrasonic beam (see "B" in Fig. 1). To take the wall filter into account, Doppler velocities of the standard solution whose magnitudes were not larger than a threshold value, $|V_{\text{WF}}|$, were zeroed as follows:

$$V' = \begin{cases} 0, & (|V| \le |V_{\text{WF}}|) \\ V, & (|V| > |V_{\text{WF}}|). \end{cases} \tag{6}$$

Considering that Doppler velocity being cut by the wall filter was 1.25%, 2.5%, 5%, or 10% of the measurable Doppler velocity, $|V_{\text{WF}}|$ was, respectively, set at four different values of 0.011, 0.022, 0.044, or 0.087 (0.4, 0.8, 1.6, or 3.2 cm/s, dimensionally). Fig. 4(b) shows the percentage of feedback points, $N_{\text{WF}}/N_{\text{FB}}$, whose Doppler velocities of the standard solution were set to be zero. The number of filtered points increases in diastole since blood flow slows down (see Fig. 2(b)).

4) Lack of Measurement Data: In ultrasonic measurement, measurement data is sometimes lacking, being displayed as zero,
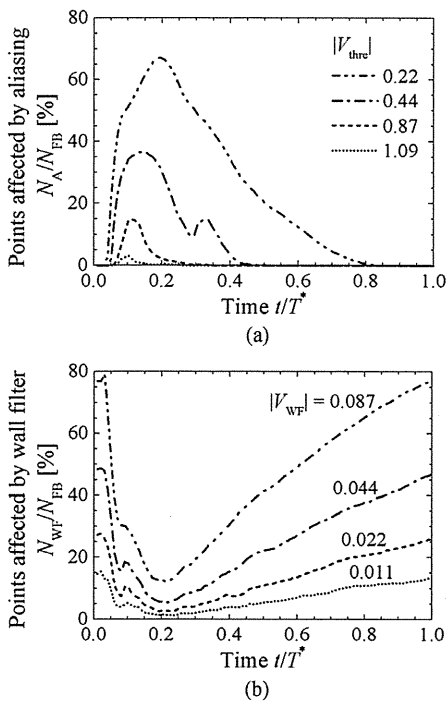
Fig. 4. Percentage of the number of grid points: (a) N_A and (b) N_{WF}, where the standard solution was affected by aliasing and wall filter, with respect to the total number of feedback points, N_{FB}, respectively.
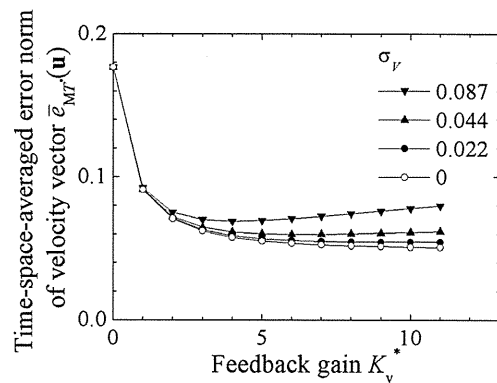

Fig. 5. Variation of time-space-averaged error norm of velocity vector of UMI simulation using the standard solution affected by Gaussian noise with feedback gain.

in cases in which the intensity of echo signals from blood cells is too small or artifacts are present (see "C" in Fig. 1). To examine the effect on UMI simulation, Doppler velocities at feedback points were randomly zeroed at a certain ratio at each time step and used for feedback. The ratio, N_{LD}/N_{FB}, of points whose Doppler velocities were lacking to all feedback points was set at four different values of N_{LD}/N_{FB} = 1%, 5%, 10%, or 20%.

D. Error Evaluation Method

For the evaluation of the computational result, space-averaged and time-space-averaged error norms of velocity vector u, $\bar{e}_M(u, t)$ and $\bar{e}_{MT^*}(u)$, based on the l_1 norm, $|u| + |v| + |w|$ for velocity vector u were calculated

$$\bar{e}_{MT^*}(\mathbf{u}) = \frac{1}{T^*} \int_{T^*} \bar{e}_M(\mathbf{u}, t) dt$$

$$= \frac{1}{T^*} \int_{T^*} \left(\frac{1}{N} \sum_n \frac{|\mathbf{u}_{cn}(t) - \mathbf{u}_{sn}(t)|}{U} \right) dt \quad (7)$$

where n and N are the index and the total number of monitoring points in the feedback domain M, respectively, and subscripts c and s, respectively, indicate the result of the UMI simulation and the standard solution. Error norms of Doppler velocity V, $\bar{e}_M(V, t)$ and $\bar{e}_{MT^*}(V)$, were also defined in the same way.

III. RESULTS AND DISCUSSION

The ability to reproduce the standard solution by UMI simulations with/without each measurement error compared with that of the ordinary simulation without feedback was evaluated

(see Table I). In the UMI simulation using the standard solution without measurement errors, the time-space-averaged error norm of the velocity vector, $\bar{e}_{MT^*}(u)$, monotonically decreased with increasing feedback gain K_v^* at an interval of 1, but the computation diverged for $K_v^* \geq 12$ (see white circle symbols in Fig. 5). Consequently, in the absence of special notations, the computational results of the UMI simulations at $K_v^* = 11$ were basically used for evaluation of the computational accuracy.

A. Effect of Gaussian Noise

Variations of the time-space-averaged error norm of the velocity vector, $\bar{e}_{MT^*}(u)$, with feedback gain, K_v^*, in the UMI simulations using the standard solution with noise ($\sigma_V = 0.022$, 0.044, 0.087) are shown with black symbols in Fig. 5. The result at $K_v^* = 0$ is the ordinary simulation without feedback. Comparison of the results at the same feedback gain indicates that the computational accuracy deteriorates as the degree of noise increases. In addition, by using the standard solution with relatively large noise such as $\sigma_V = 0.087$, the computational accuracy of UMI simulation becomes worse with increasing feedback gain. However, within the degree of noise in this study, the error in the UMI simulation become smaller than that in the ordinary simulation ($K_v^* = 0$) in all conditions, implying the improvement of the computational accuracy.

For each UMI simulation using the standard solution with noises of $\sigma_V = 0.011$, 0.022, 0.044 and 0.087, optimum feedback gain, at which $\bar{e}_{MT^*}(u)$ became the smallest, was obtained as $K_v^* = 11$, 10, 6, and 4, respectively. Hereafter, in this subsection, the computational accuracy of the UMI simulation at each optimum feedback gain is investigated in greater detail. Fig. 6(a) compares space-averaged error norms of Doppler velocity, $\bar{e}_M(V, t)$, between UMI simulations using the standard solution without noise ($\sigma_V = 0$, dotted line) and with noise of $\sigma_V = 0.044$ (dashed line), the standard solution with the noise of $\sigma_V = 0.044$ (gray line), and the ordinary simulation (black line). Deviances in Doppler velocity of the standard solution due to noise leads $\bar{e}_M(V, t)$ of the UMI simulation to somewhat increase. However, the value is smaller than that of the ordinary simulation, showing that even the UMI simulation with noise